Experimental constraints on dacite magma storage beneath Volcán Quizapu, Chile

Emily C. First*[1,3,4], Julia E. Hammer[1], Philipp Ruprecht[2], and Malcolm Rutherford[3]

1 University of Hawai‘i at Mānoa, Department of Earth Sciences, Honolulu, HI 96822

2 University of Nevada, Reno, Department of Geological Sciences & Engineering, Reno, NV 89557

3 Brown University, Department of Earth, Environmental & Planetary Sciences, Providence, RI 02912

4 Cornell University, Department of Earth & Atmospheric Sciences, Ithaca, NY 14853

*Corresponding author: efirst@cornell.edu

Running title: Magmatic storage conditions, Volcán Quizapu

© The Author(s) 2021. Published by Oxford University Press. All rights reserved. For Permissions, please e-mail: journals.permissions@oup.com

Downloaded from https://academic.oup.com/petrology/advance-article/doi/10.1093/petrology/egab027/6188641 by University of Nevada at Reno user on 31 March 2021

ABSTRACT

Volcán Quizapu, Chile, is an under-monitored volcano that was the site of two historical eruptions: an effusive eruption in 1846-1847 and a Plinian eruption in 1932, both of which discharged ~5 km^3 (DRE) of lava and/or tephra. The majority of material erupted in both cases is trachydacite, nearly identical for each event. We present H_2O-saturated, phase equilibrium experiments on this end-member dacite magma, using a pumice sample from the 1932 eruption as the main starting material. At an oxygen fugacity (fO_2) of ~NNO+0.2, the phase assemblage of An_{25-30} plagioclase + amphibole + orthopyroxene, without biotite, is stable at 865±10 °C and 110±20 MPa H_2O pressure (P_{H2O}), corresponding to ~4 km depth. At these conditions, experiments also reproduce the quenched glass composition of the starting pumice. At slightly higher P_{H2O} and below 860 °C, biotite joins the equilibrium assemblage. Because biotite is not part of the observed Quizapu phase assemblage, its presence places an upper limit on P_{H2O}. At the determined storage P_{H2O} of ~110 MPa, H_2O undersaturation of the magma with $X_{H2O}^{fluid} = 0.87$ would align P_{total} to mineral-based geobarometry estimates of ~130 MPa. However, $X_{H2O}^{fluid} < 1$ is not required to reproduce the Quizapu dacite phase assemblage and compositions. A second suite of experiments at lower fO_2 shows that the stability fields of the hydrous silicates (amphibole and biotite) are significantly restricted at NNO-2 relative to NNO+0.2. Additional observations of Quizapu lava and pumice samples support the existing hypothesis that rapid pre-eruptive heating drove the effusive 1846-1847 eruption, with important refinements. We demonstrate that microlites in the end-member dacite lavas are consistent with *in situ* crystallization (during ascent), rather than transfer from an andesite. In one end-member dacite lava, newly identified reverse zoning in orthopyroxene and incipient destabilization of amphibole are consistent with small degrees of heating. Our work articulates a clear direction for future Quizapu studies, which are warranted given the active nature of the Cerro Azul-Descabezado Grande volcanic axis.

Downloaded from https://academic.oup.com/petrology/advance-article/doi/10.1093/petrology/egab027/6188641 by University of Nevada at Reno user on 31 March 2021

INTRODUCTION

Two major historic eruptions have issued from what is now known as Quizapu crater, a flank vent on Cerro Azul stratovolcano in the Andean Southern Volcanic Zone. Both eruptions emitted 4-5 km^3 of dacitic material of ~67 wt.% SiO_2 (Hildreth & Drake, 1992; Ruprecht *et al.*, 2012). However, the eruption in 1846-1847 consisted of lava effusion, whereas the eruption in 1932 was a Plinian event (Hildreth & Drake, 1992). This dramatic difference in eruptive style has already motivated a suite of studies (Ruprecht & Bachmann, 2010; Ruprecht & Cooper, 2012; Ruprecht *et al.*, 2012; Higgins *et al.*, 2015; Degruyter *et al.*, 2017; Fiege *et al.*, 2017). The present effort is focused on constraining the long-term pre-eruptive storage conditions of the dacite magma. Because the dominant phase assemblage and phase compositions are essentially identical for 1846-1847 lava and 1932 pumice, our work applies to both eruptions, providing a robust baseline from which pre- and syn-eruptive processes can be analyzed for the past eruptions and during similar eruptive crises in the future.

Volcán Quizapu is located in the Maule region of Chile, roughly 300 km south of Santiago (Figure 1). The surrounding volcanic field is host to at least 12 Holocene vents and/or eruptive deposits, which range from basalt to rhyolite (Hildreth & Drake, 1992). Cerro Azul itself is a composite cone with basal flows < 400 ka, with eruptive products spanning nearly the entire compositional range of the volcanic field (Drake, 1976; Hildreth & Drake, 1992). Less than 10 km to the north is the edifice of Descabezado Grande, a similar-aged stratovolcano (Figure 1). Cerro Manantial Pelado to the northwest is a unique mafic stratovolcano that records prolonged storage of primitive magmas even in the thick arc crust of the Southern Volcanic Zone (Winslow et al., 2020). The craters of La Resolana to the west, and Los Hornitos cinder cones to the south are shorter-lived mafic centers (Salas *et al.*, 2017). The 150-800 ka Loma Seca Tuff forms a large plateau at the eastern end of the field, with the associated Calabozos caldera to the northeast (Hildreth *et al.*, 1984; Grunder & Mahood, 1988). Basement rocks of the Miocene Invernada pluton are exposed to the southeast (Drake, 1976). There is some evidence for interconnectivity of volcanic centers in the region, likely due to faulting associated with the dextral transpressional stress regime along the arc (Cembrano & Lara, 2009; Salas *et al.*, 2017). In addition, 2-3 months after the Plinian eruption of Quizapu in 1932, a 600-m wide crater appeared on the north flank of Descabezado Grande (Fuenzalida, 1942), essentially along an axis linking Cerro Azul, the Quizapu vent, and Descabezado Grande. Although no juvenile material was expelled, ash plumes several

http://www.petrology.oupjournals.org/

Downloaded from https://academic.oup.com/petrology/advance-article/doi/10.1093/petrology/egab027/6188641 by University of Nevada at Reno user on 31 March 2021

kilometers high were visible sporadically for months (Hildreth & Drake, 1992) and lithic-dominated ejecta line the crater. Thus, despite the homogeneity of eruptive products at Quizapu itself, the surrounding region, even within ~10 km, contains lavas and tephra that span the gamut of calc-alkaline compositions. Determining the long term storage temperature and pressure of the Quizapu dacite magma is a necessary starting point from which to model and understand any past or potential future interactions between it and the region's diverse magmas.

Dacitic magma from the first, chiefly effusive, eruption at Quizapu (1846-1847) demonstrably interacted with a more mafic end-member. The compositions of individual flows range from homogeneous dacite to hybridized dacite-andesite mixtures. In many flows, enclaves of andesite (54-58 wt.% SiO_2; Ruprecht *et al.*, 2012) provide evidence for the involvement of more mafic material. Ruprecht & Bachmann (2010) postulate that this andesitic magma was volumetrically significant enough (10-45 vol.% of most flows) to both trigger the 1846-1847 eruption and heat parts of the main dacite body. In their analysis, this excess heat would have reduced the dacite viscosity enough to allow passive outgassing of excess volatiles. Minor mafic scoria is also associated with the explosive 1932 eruption, but to a far lesser volumetric extent (< 5% of the deposit). This less evolved magma is mainly evident in three intervals in the fall deposit: an initial andesite scoria that grades via banded pumice to the dominant dacite, an intraplinian "brown band" of andesite and banded pumice, and a terminal basalt-andesite scoria layer (Hildreth & Drake, 1992). Minor rhyodacite (69-70 wt.% SiO_2) also erupted during the Plinian event, accounting for <0.5 vol.% of the deposit (Hildreth & Drake, 1992). Thus, mafic-silicic magma interaction is evident in products from the 1932 Plinian eruption, but the mafic contribution was not significant enough to affect the overall dacite magma body in terms of composition, or presumably heat transfer (Ruprecht & Bachmann, 2010), as it was in the 1846-1847 event.

Hildreth & Drake (1992) give a first overview of the Quizapu dacite petrology, expanded upon by Ruprecht *et al.* (2012) and Higgins *et al*. (2015). We briefly summarize here. End-member dacites from both the 1846-1847 and 1932 eruptions are indistinguishable in terms of phase assemblage and bulk composition (Figure 2; Table 1). They consist of ~15-20 vol.% phenocrysts, mainly An_{25-40} plagioclase, with ~2 vol.% each amphibole (dominantly magnesiohornblende) and orthopyroxene (En_{65-77}, $Wo_{<3}$). Subordinate clinopyroxene, titanomagnetite, ilmenite, apatite, and sulfide blebs each make up <1 vol.% of the material. Biotite has never been reported in the Quizapu dacite. Pumice clasts from 1932 lack microlites. Many 1846-1847 lavas contain microlites of

Downloaded from https://academic.oup.com/petrology/advance-article/doi/10.1093/petrology/egab027/6188641 by University of Nevada at Reno user on 31 March 2021

plagioclase, estimated as An_{30-60} (Ruprecht *et al.*, 2012). The origin of these microlites has been attributed to transfer from an andesitic recharge magma (Ruprecht & Bachmann, 2010; Ruprecht *et al.*, 2012), a point we address below in the section titled "Refinements to the pre-eruptive heating hypothesis." Some sections of the flows are glassy dacite with scant microlites.

Using petrologic models, the above phase assemblage has been linked to a set of magma storage conditions. Temperature and oxygen fugacity (fO_2) estimates based on the compositions of Fe-Ti oxides or amphibole are broadly in agreement, converging around 835-885 °C and NNO+0.5 to NNO+1 (Hildreth & Drake, 1992; Ruprecht & Bachmann, 2010; Ruprecht *et al.*, 2012), although some Fe-Ti oxide pairs in the 1846-1847 end-member (i.e., homogeneous) dacite yield temperatures up to 956 °C (Ruprecht *et al.*, 2012). Storage pressures are based on amphibole barometry, and range from 120-180 MPa (method of Ridolfi & Renzulli, 2012 as reported in Ruprecht *et al.*, 2012). The H_2O content of the magma is estimated at 3.5-5.5 wt.% using amphibole compositions (method of Ridolfi & Renzulli, 2012 as reported in Ruprecht *et al.*, 2012), or a slightly higher range of 4-6 wt.% H_2O using plagioclase-liquid hygrometry (method of Lange *et al*., 2009, as reported in Ruprecht *et al.*, 2012). For comparison, the associated andesitic recharge magma, assessed via mafic enclaves in hybridized magmas, records an fO_2 of NNO+0.2 to NNO+0.5 and a temperature of ~1100 °C, with pressure unknown but likely to be >300 MPa (Ruprecht *et al.*, 2012).

Because ambient magmatic conditions prior to unrest and eruption are the critical baseline from which all perturbations and syn-eruptive processes are evaluated, determining these conditions for the Quizapu system is essential. Although the pressure, temperature, H_2O, and fO_2 estimates derived from the natural Quizapu dacite phases are reasonable, laboratory experiments are capable of refining the nature of the pre-eruptive storage region and are not susceptible to errors introduced by extrapolating beyond the datasets on which geothermometers and geobarometers are calibrated. For example, Quizapu amphibole crystals contain more Al in tetrahedral coordination and more Cl than the vast majority of crystals used to derive the chemometric equations of Ridolfi & Renzulli (2012) (Figure S1). Here, we present a suite of H_2O-saturated phase equilibrium experiments aimed at sharpening constraints on the storage conditions of the dacite magma prior to the 1932 eruption. These conditions are inferred to apply as well to the magmatic system before the 1846-1847 eruption, based on the near-identical dacite erupted.

Downloaded from https://academic.oup.com/petrology/advance-article/doi/10.1093/petrology/egab027/6188641 by University of Nevada at Reno user on 31 March 2021

METHODS

Starting materials and experimental strategy

Our experiments were designed to examine in detail two principal variables, temperature and pressure, under H_2O-saturated conditions ($P = P_{H2O}$). Water saturation is a common simplifying assumption for initial experimental work on dacite-to-rhyolite magmas at subduction zones, as it often results in successful reproduction of natural phase assemblages and compositions without the need to call upon X_{H2O}^{fluid} (mole fraction H_2O in the exsolved volatile phase) as an additional variable (e.g., Castro *et al.*, 2013; Grocke *et al.*, 2017). Furthermore, there are no existing analyses of melt inclusion volatile contents for Quizapu to suggest a more definitive X_{H2O}^{fluid}, a recent thermomechanical model requires a free fluid phase to explain the Quizapu eruption styles (Degruyter *et al.*, 2017), and the presence of amphibole implies a relatively high melt water content (e.g., Rutherford & Devine, 1988; Riker *et al.*, 2015). Our experiments at $X_{H2O}^{fluid} = 1$ are therefore a reasonable approach for the first experiments on this magmatic system, and indeed reproduce the natural phase assemblage (Results). Magmatic oxidation state is also susceptible to change, for example by mixing with a more reduced magma (e.g., Tomkins *et al*., 2012), and we explore the effects of fO_2 on phase equilibrium, in a broad-brush way. The mafic enclaves and their host lavas from Quizapu record an fO_2 nearly 0.5 log units lower than that recorded by end-member dacites (Ruprecht *et al.*, 2012), cementing the value of this additional investigation.

Two sets of experiments were conducted: one at an fO_2 close to that determined for Quizapu and other intermediate arc magmas (NNO to NNO+1) and one at a lower fO_2 (NNO-2). We draw on the former set, the "high fO_2" suite, for insights and conclusions about the Quizapu magmatic system specifically, and it is the main focus of our study. The "low fO_2" suite complements the high-fO_2 experiments by indicating the direction of phase equilibrium shifts due to a change in dacite oxidation state, such as may be induced by mixing and degassing of a mafic magma into overlying dacite (Pallister *et al*., 1996; Kress, 1997). All but three of the high fO_2 experiments were conducted at Brown University, as described below (Table 2). The low fO_2 experiments and three of the high fO_2 experiments (QDeq34-36) were conducted at the University of Hawaii (UH; Table S1). Details for the low fO_2 experiments are reported in the Supplementary Methods. The key methods and materials were identical to those for the high fO_2 suite, described below, except for the addition of lava VQ-06-06 as a starting material (nearly isochemical with pumice VQ-07-37D), and the composition of the pressurizing medium imposing the lower fO_2.

Downloaded from https://academic.oup.com/petrology/advance-article/doi/10.1093/petrology/egab027/6188641 by University of Nevada at Reno user on 31 March 2021

Microlite-free pumice VQ-07-37D, erupted in 1932, served as the initial starting material for all high fO_2 experiments. This pumice was crushed and sieved to <1.4 mm, then lightly crushed again to reduce volume but leave crystals intact, thus largely isolating crystal cores from the reactive assemblage (Pichavant *et al.*, 2007). Aliquots of 0.2-0.3 g were loaded into 5 mm outer diameter (O.D.) Ag or $Ag_{60}Pd_{40}$ capsules. Prior to loading the starting material, enough deionized water was added to each capsule to exceed saturation for rhyolite (Moore *et al.*, 1998), typically 5-10 wt.% H_2O added depending on experimental pressure (35-200 MPa). Water saturation values calculated from quenched experimental melt fractions range from ~2-6 wt.% (Zhang *et al*., 2007). Capsules were crimped to a triple junction, then sealed using either an oxyacetylene welding torch or a tungsten inert gas impulse micro welder. In two experiments, secondary capsules of 3 mm O.D. ("B" capsules) were filled with material from experiments previously run at higher temperature and pressure, crimped shut without welding, and placed inside the 5 mm capsule containing the initial starting material ("A" capsule). These experiments approached equilibrium from two directions, such that overall, the A material melted to reach equilibrium, and the B material crystallized. Previously run experiments were also used as starting materials in eight of the single-capsule experiments (Table 2), providing a variety of equilibration pathways.

All experiments were conducted in horizontal clamshell furnaces with Waspaloy vessels and Ni filler rods, using a cold-seal water-medium pressure line. Both dark grey Ni and green NiO were visible on the filler rod or in the vessel at the end of each run. Temperature was monitored with Omega K-type thermocouples (± 6.4 °C). Pressure was monitored with a Heise mechanical pressure gauge (± 0.5 MPa). The experimental setup employed has a well-established intrinsic fO_2, set by the vessel, NiO-encrusted Ni filler rods, and pressurizing H_2O. Reported conditions range from NNO-0.3 (Muir *et al.*, 2014) to NNO+1 ± 0.5 (Geschwind & Rutherford, 1992; Gardner *et al.*, 1995). Our own determination of pressure line fO_2 at UH, assessed with a CoPd solid-state sensor (Taylor *et al.*, 1992), revealed an fO_2 of NNO+0.2, broadly consistent with Fe-Ti oxide compositions indicating an fO_2 of NNO-0.1 to NNO+0.7 (Figure S2, Figure S3; Ghiorso & Evans, 2008; Ghiorso & Prissel, 2020). Run durations varied from 1 to 14 days, and quenches were performed by air-cooling the vessel for ~20 seconds and then plunging it into a bucket of water, while pressurized. The samples are estimated to cool by 300 °C within 6 s (Brugger & Hammer, 2010), rapidly bringing samples underneath the glass transition. Seven experiments contain crystal phases near capsule walls that contain Ni above the trace levels expected with 4 ppm Ni in bulk

Downloaded from https://academic.oup.com/petrology/advance-article/doi/10.1093/petrology/egab027/6188641 by University of Nevada at Reno user on 31 March 2021

pumice VQ-07-37D (Ruprecht *et al.*, 2012). This phenomenon is likely due to an influence of the pressurizing medium (water in the presence of Ni and NiO) during the quench process. See Supplementary Methods for additional discussion. The glasses in these experiments fall within expected compositional trends, and phases present only in these outer edge regions or contaminated with Ni were not used to constrain the phase diagram or specific phase compositions.

Two short experiments (both at 920 °C) were run in a cold-seal, gas-medium pressure line in a sheathed TZM vessel (Brown University), to access combinations of pressure and temperature not sustainable by Waspaloy vessels. These experiments included Ni – NiO buffers in an outer capsule to ensure that the fO_2 inside the sample capsule did not rise far above the NNO buffer, as is the tendency when H_2 diffuses out of the experimental capsule into the surrounding argon atmosphere (Shea & Hammer, 2013a). Both experiments used argon as the pressurizing medium, and one incorporated methane in the pressure ratio 1 CH_4 : 16 Ar to help offset the expected oxidation. Quench of these TZM runs was accomplished by plunging the sheath and pressurized vessel directly into a bucket of water.

At the end of each experiment, a small hole was clipped in the capsule to listen for the sound of escaping gas, assuring us that the run had been H_2O-saturated. Capsules were then peeled open and experimental samples collected. Thin or thick sections of each sample were polished with SiC and alumina papers and slurries, down to 0.3 or 0.05 microns. These sections were examined under reflected and/or transmitted light and then carbon coated for electron probe analysis.

Electron microscopy

The experimental sample suites were imaged and analyzed with the Cameca SX-100 electron microprobe at Brown University (high fO_2 suite, except QDeq34-36), and with the JEOL Hyperprobe JXA-8500F electron microprobe at the University of Hawaii (low fO_2 suite, natural samples, and QDeq34-36). Rapid, qualitative compositional information for sample description and phase identification was obtained using energy dispersive spectrometry (EDS). Glass, plagioclase, amphibole, pyroxene, Fe-Ti oxide, and biotite spot compositional analyses were acquired using wavelength-dispersive spectrometry (WDS), with a 15 keV accelerating voltage for all phases except Fe-Ti oxides (20 kV). High and low off-peak counting times were each half of the on-peak time. Matrix corrections use either PAP procedures (Pouchou & Pichoir, 1991) or the Armstrong/Love Scott algorithm (Armstrong, 1988), depending on the built-in data reduction

http://www.petrology.oupjournals.org/

Downloaded from https://academic.oup.com/petrology/advance-article/doi/10.1093/petrology/egab027/6188641 by University of Nevada at Reno user on 31 March 2021

routine. See Tables S2 and S3 for all data, including analyses of standards used to monitor drift and assess analysis reproducibility. Below, we summarize data collection for each phase. Extensive additional information, including standards used for each calibration, is detailed in the Supplementary Methods,

Glass analyses used a 10 nA beam current and 5-15 μm beam diameters, depending on the size of the crystal-free area. On-peak counting times for glass spots ranged from 30-65 s depending on the element (Si, Ti, Al, Fe, Mn, Mg, Ca, Na, K, P, Cl). An automated time-dependent intensity correction was applied to all analyses to account for Na mobility under the beam. Repeated analyses of multiple synthetic glasses and BCR-2G (USGS) were used to assess reproducibility and correct for analytical drift.

Plagioclase analyses used a 10 nA beam current and beam diameters ranging from focused to 1 μm due to the small size of experimental microlites and rims. On-peak counting times were 45-90 s for measured elements (Si, Ti, Al, Fe, Mg, Ca, Na, K). Repeated analyses of Lake County plagioclase were used to assess reproducibility and correct for analytical drift. Time-dependent intensity corrections were applied to Na data, except in limited cases where Na counts were constant over time.

Amphibole and pyroxene analyses used 10-15 nA beam currents and spot sizes ranging from focused (< 1 μm) to 10 μm. Biotite analyses used the same calibrations, but at 5 nA. On-peak counting times were 40-60 s for all elements (Si, Ti, Al, Cr, Fe, Mn, Mg, Ni, Ca, Na, K, Cl, F). Repeated analyses of Kakanui hornblende (NMNH 143965) and Lunar Crater augite (NMNH 164905) or diopside (USNM 117733) and VG-2 glass (NMNH 111240-52) were used to assess reproducibility and correct for analytical drift. Amphibole formulas were calculated based on the standard formula $A_{0-1}B_2C_5T_8O_{22}(OH,F,Cl)_2$, using a 23(O) basis and assuming 2(OH, Cl, F) (Leake, 1978). Two schemes were averaged to arrive at the final formulas prior to site assignment: sum to 13 cations excluding Ca, Na, and K; sum to 13 cations excluding Ca, Na, K, and Mn (Robinson *et al.*, 1982). H_2O and F (where necessary) were calculated by difference, for site assignments and assessment of analysis totals.

Analyses of Fe-Ti oxides used 25 nA beam currents (at 20 kV), with spot sizes ranging from focused (< 1 μm) to 5 μm. On-peak counting times were 30-65 s (Si, Ti, Al, Cr, Fe, Mn, V, Mg). Repeated analyses of both sphene glass and chromite USNM 117075 were used to assess and correct for analytical drift. Corrections were applied for the interference of Cr on Mn and of Ti on

http://www.petrology.oupjournals.org/

Downloaded from https://academic.oup.com/petrology/advance-article/doi/10.1093/petrology/egab027/6188641 by University of Nevada at Reno user on 31 March 2021

V (Donovan *et al.*, 1993), using interference standards Cr_2O_3 (Cr) and sphene glass (Ti). Analyses were re-calculated to account for Fe speciation, using the method of Droop (1987).

Interlaboratory agreement of EPMA analyses between Brown University and the University of Hawaii has been demonstrated in a recent study, wherein mafic glass from a single experimental thin section was analyzed at both Brown and UH (sample R04C; First *et al.*, 2020). The average compositions from each lab are in good agreement. With the exception of P_2O_5, which matches within the 2σ range, any discrepancies fall within the overlap of 1σ variability for the two sets of analyses.

RESULTS

Natural samples

Pumice VQ-07-37D and lava VQ-06-06 are both trachydacites, based on whole rock compositions (Table 1), and residual glass in both samples is rhyolitic (Figure 3). A point count of the VQ-06-06 lava shows 75 vol.% groundmass, 21 vol.% plagioclase, 2 vol.% amphibole, 1 vol.% pyroxene, 1 vol.% opaques, and <1 vol.% apatite (Figure S4). These proportions are in broad agreement with published estimates, although the amount of plagioclase ranges widely (Hildreth & Drake, 1992; Ruprecht *et al*., 2012; Higgins *et al.*, 2015).

Analyses of amphibole in VQ-06-06 are consistent with previous work (Ruprecht *et al.*, 2012; Table S2). Orthopyroxene compositions of $En_{62\text{-}70}Wo_{2\text{-}3}$ also overlap those previously reported (Table S2; Hildreth & Drake, 1992; Ruprecht *et al.*, 2012). Within this range, subtle reverse zoning of orthopyroxene occurs in lava VQ-06-06 (Figure 4c-d, Figure 5). These orthopyroxene crystals also display fine growth features on some faces. In pumice VQ-07-37D, individual orthopyroxene grains are unzoned and subhedral, with a composition matching the rims of orthopyroxene grains in the lava (Figure 4b). Glomerocrystic grains display irregular, non-concentric zoning (Figure S5).

Plagioclase phenocrysts in both lava and pumice are texturally similar to the descriptions in Ruprecht et al. (2012), dominated by subhedral crystals with "weak patchy zoning" and uncommon melt inclusions (akin to type IA of Ruprecht *et al.*, 2012). Chemical analyses of plagioclase in VQ-07-37D pumice average An_{36} but represent a limited sampling. Plagioclase microlites in the lava (Figure 6e) are typically ~An_{20}, with a range of An_{18}-An_{43}. They commonly display hourglass zoning (Figure S6).

http://www.petrology.oupjournals.org/

Downloaded from https://academic.oup.com/petrology/advance-article/doi/10.1093/petrology/egab027/6188641 by University of Nevada at Reno user on 31 March 2021

Fe-Ti oxides in both the lava and the pumice have end-member compositions of $Mt_{68}Usp_{32}$ for the spinel phase ("magnetite") and $Hm_{15}Ilm_{85}$ for the rhombohedral phase ("ilmenite") (Table S2; recalculation scheme of Buddington & Lindsley, 1964), which are similar to those previously reported for the same samples (Ruprecht *et al.*, 2012), though significantly lower in V and Mn (Figure S7c-d; see Discussion). Calculated T-fO_2 conditions (Figure 7; via Ghiorso & Evans, 2008) fall within and slightly below published ranges (Hildreth & Drake, 1992; Ruprecht *et al.*, 2012). We note three previously unrecognized features: (1) subtle zoning in both magnetite and ilmenite from lava VQ-06-06 (Figure 8a-b; Figure S7a-b), which we interpret to represent alteration of pre-existing crystals in the cooling lava flow, perhaps due to fluid percolation; (2) magnetite with fine-scale, crystallographically controlled oxyexsolution in pumice VQ-07-37D (Figure 8c), probably representing a syn- to post-eruptive process such as rapid oxidation upon cooling exposed to atmospheric conditions (Lattard *et al.*, 2012); (3) in both lava and pumice, a nearly pure Fe oxide phase with extreme rounding and pervasive melt pockets (Figure 8d), which is interpreted as the remnants of iron sulfide globules that destabilized as degassing of S-bearing fluids occurred during ascent. A similar interpretation is put forth for "spongy" Fe oxide occurrences in intermediate to felsic magmas at other volcanoes, including Satsuma-Iwojima, Japan (Larocque *et al.*, 2000; see their Fig. 2E) and Mount Pinatubo, Philippines (Di Muro *et al.*, 2008). Thus, while these features may be revealing of syn- and post-eruptive processes, they are not indicative of long-term storage conditions, and indeed are absent from experimental run products.

Experimental samples

Attainment of equilibrium

Twenty-four experiments were run at static P-T conditions above the NNO buffer (~NNO+0.2), and 47 were run at NNO-2. The experiments in this study are of the "partial equilibrium" type described by Pichavant *et al.* (2007), meaning that the expectation of equilibrium is limited to melt, phenocryst rims, and microlites. Total equilibrium experiments using a powdered bulk starting material would not yield appropriate results, because phenocrysts in arc magmas may have experienced a range of conditions prior to their residence in the pre-eruptive magma chamber. Thus, phenocrysts were intentionally left intact to prevent interaction of melt with crystal cores (Hammer, 2008). Using a synthetic material necessitates either superheating, which affects phase textures and compositions (First *et al.*, 2020; First & Hammer, 2016), or risking that the material does not homogenize prior to experimentation. Given these constraints,

Downloaded from https://academic.oup.com/petrology/advance-article/doi/10.1093/petrology/egab027/6188641 by University of Nevada at Reno user on 31 March 2021

natural starting material was used, and partial equilibrium experiments were performed. Due to the unreacted crystal cores retained in these experiments, mineral modes are unreliable comparative indicators, and natural-experimental matches are assessed via phase assemblage, texture, and composition. Microprobe analysis was performed on rims, growth protuberances, and microlites – features likely to have been grown or modified during the experiments.

Experiment durations of 7-14 days are in line with similar partial equilibrium experiments on moderately silicic magmas (Rutherford & Devine, 1996; Hammer *et al.*, 2002; Costa *et al.*, 2004). Shorter experiments were also run, generally due to their higher temperature (≥ 890 °C) or a desire to check for specific features (e.g., amphibole breakdown) before continuing longer. Regardless of duration, compositional homogeneity of the glass is an indicator of a close approach to equilibrium of crystal margins and melt. Our experimental glass compositions display robust trends with changes in temperature and pressure, and on average have a relative standard deviation of ≤ 5% for all major elements. Samples run for less than seven days are not systematically less homogeneous than samples run for a week or longer. In a time series (QZ120 and QZ121) run for two days and then an additional six days, the glass composition changed by < 1% relative in SiO_2, Al_2O_3, and Na_2O (Table 3). Double capsule experiments run with two different starting materials simultaneously (reversals) converged on similar final states in terms of phase presence and composition (Figure S8), indicating a good approximation to equilibrium (e.g. Wyllie *et al.*, 1981; Médard & Grove, 2008).

Below, unless otherwise indicated, experimental details and related interpretations of the Quizapu magma storage conditions are based on experiments run at ~NNO+0.2, which closely replicate the oxidation state of the natural dacite samples.

Plagioclase

Plagioclase phenocrysts and crystal fragments, with varied textures and compositional zoning, were inherited from the starting material. Plagioclase microlites grew in experiments run at lower pressure-temperature conditions than those of their immediate starting material (Figure 6a-d). Distinct rims, interpreted as new growth, are common in these same experiments (Figure 6a-b), but are rare and more discontinuous in other charges. In such experiments at higher pressures and temperatures (i.e., above the shaded region in Figure 6f), new growth is more difficult to establish with certainty, so plagioclase compositional analyses are less systematic and fewer were attempted. For experimental plagioclase, there is a general trend of increasing anorthite content

http://www.petrology.oupjournals.org/

Downloaded from https://academic.oup.com/petrology/advance-article/doi/10.1093/petrology/egab027/6188641 by University of Nevada at Reno user on 31 March 2021

(An) with increasing temperature and P_{H2O}. Plagioclase compositions of the experimental set overlap those of the Quizapu pumice (An_{25-30}) in a band stretching from approximately 810 °C at 200 MPa to 890 °C at 90 MPa (Figure 6f).

Fe-Mg Silicates

Above a curve from ~70 MPa at 830 °C to ~90 MPa at 875 °C, amphibole is present as euhedral phenocrysts and microphenocrysts that resemble those in the starting material and as small (~10-30 μm), faceted crystals that are consistent with syn-experimental nucleation and growth (Figure S9). On (micro)phenocrysts, rims of contrasting composition are common and also consistent with syn-experimental growth (Figure 9c-d). These rims tend to be thicker at corners and are not uniformly continuous. Below ~70 MPa or above ~910 °C, amphibole is unstable. Relict grains are rounded and surrounded by melt. Some of these same grains are associated with low-Ca pyroxene crystals, either in direct contact with the outgoing amphibole or adjacent to it (Figure 9e-f). Amphibole rim compositions change inconsistently with experimental conditions, at some pressures (e.g., 125 MPa) displaying coherent trends with temperature and at others (e.g., 150 MPa) appearing more variable (Figure S10). Most samples contain experimentally grown amphibole across a range of composition, with different elements matching the Quizapu magnesiohornblende composition at different conditions. There is not a specific experiment that produces a best match to the natural amphibole composition; rather many experiments contain amphibole compositions consistent with those in the Quizapu dacite (Figure S10). The compositional complexity and relatively low abundance of amphibole in these experiments preclude using its composition as a more specific indicator of natural-experimental match conditions.

Low-Ca pyroxene is a stable phase in the 14 experiments falling outside of the biotite stability field. At low pressures and temperatures it grows on or near relict amphibole, as well as in the groundmass. At higher pressures, low-Ca pyroxene is frequently subhedral, occasionally associated with high-Ca pyroxene and/or amphibole. At 920 °C, discontinuous growth protrusions on low-Ca pyroxene crystals are enriched in Mg relative to the crystal cores. At pressures >90 MPa and temperatures <850 °C, low-Ca pyroxene is unstable, with anhedral grains surrounded by biotite, or biotite plus high-Ca pyroxene or amphibole (Figure 10b-d). High-Ca (clino)pyroxene is less abundant in both the starting pumice and the experimental set in general, and its presence is inconsistent in pressure-temperature space. E.g., in one experiment that cooled to atmospheric

Downloaded from https://academic.oup.com/petrology/advance-article/doi/10.1093/petrology/egab027/6188641 by University of Nevada at Reno user on 31 March 2021

temperature and lost pressure (QZ115), high-Ca pyroxene grew on unstable amphibole remnants and remained after a subsequent 12 days at the intended temperature and pressure (875 °C, 75 MPa). This metastable persistence of clinopyroxene is reflected in the anomalously evolved quenched melt composition of this sample (Table 3). It is consistent with slow silicate phase reactions in similar arc dacites (e.g., Hammer & Rutherford, 2003), and explains the unpredictability of this minor phase across the experimental space examined here (Table 2).

Biotite formed as a stable phase at nine pressure-temperature combinations (Table 2), surrounding anhedral low-Ca pyroxene crystals and/or as a groundmass phase (Figure 10). Euhedral, tabular crystals are most common, with subordinate triangular to hexagonal cross-sections. Most crystals are <5 μm wide. Biotite crystals also formed at the front of a zone of enhanced crystallization at the outer edge of some experimental charges (Figure S11). These areas are interpreted as zones of quench crystallization and are not considered indicative of the long-term experimental phase assemblages.

Accessory phases

Fe-Ti oxides are present in all experimental run products. Titanomagnetite is stable in all experiments, and hemoilmenite is stable in experiments below ~890 °C. A spinel phase grew in QZ122, at 920 °C, 161 MPa. Fe-Ti oxide compositions were measured in three experiments (QDeq34-36; Table S2) that contain plagioclase of An_{25-30}. Many grains were on the order of 1-10 μm in the plane of section, resulting in mixed analyses or low totals. For analyses with acceptable totals, all measured titanomagnetite and hemoilmenite spots are in Mg-Mn equilibrium in a given sample (Figure S2; Bacon & Hirschmann, 1988). The Fe-Ti oxides in these samples bracket the composition of the pumice Fe-Ti oxides ($Mt_{68}Usp_{32}$ and $Hm_{15}Ilm_{85}$). Application of the Ghiorso & Evans (2008) geothermobarometer gives Fe-Ti exchange temperatures averaging 814 °C for QDeq34 (T_{expt} = 860 ± 6.4 °C) and 827 °C for QDeq36 (T_{expt} = 810 ± 6.4 °C) (Figure S3; Ghiorso & Prissel, 2020). Temperature errors using this thermometer approach 50 °C when a small number of analyses are used (Jolles & Lange, 2019), so these results are not inconsistent with experimental conditions. Apatite is ubiquitous as an accessory phase, with morphologies ranging from skeletal to fully faceted, hexagonal to elongate (Figure S12). Iron sulfides are observed in one experiment, while many charges contain AgS, the result of incorporation of small amounts of the noble metal (Ag and $Ag_{60}Pd_{40}$) capsule material.

http://www.petrology.oupjournals.org/

Downloaded from https://academic.oup.com/petrology/advance-article/doi/10.1093/petrology/egab027/6188641 by University of Nevada at Reno user on 31 March 2021

Glass

Residual glass compositions across the experimental spectrum display well-defined element trends with both temperature and pressure, except in trace components MnO, P_2O_5, and Cl (Figure 11; Figure S13; Table 3). These trends indicate a range of conditions over which experiments match the glass composition of Quizapu pumice (Figure 12). Experimental glasses are reasonably homogeneous, with typical standard deviations of 5% relative or better for six of the eight major and minor components (e.g., relative standard deviation of 0.5% for SiO_2, 1.3% for Al_2O_3, 4.4% for FeO). Compositional trends positively correlate with both temperature and pressure for TiO_2, Al_2O_3, FeO, MgO, CaO, and Na_2O, although TiO_2 is poorly correlated with pressure. Silica and K_2O define negative trends with both temperature and pressure. Although nearly all compositional components are well described by linear trends with temperature and pressure (Figure 11), some deviations are expected due to significant phase changes, like the introduction of biotite (K) or ilmenite (Ti). However, these phases are present in such small amounts that instead of manifesting as major slope breaks in associated glass data, they simply add irregularity to the trends (Figure S13).

Downloaded from https://academic.oup.com/petrology/advance-article/doi/10.1093/petrology/egab027/6188641 by University of Nevada at Reno user on 31 March 2021

DISCUSSION

Assessing long-term storage conditions

Criteria

Using our experiments to extract a best estimate of magmatic storage conditions for the Quizapu dacite requires that the key features of the natural magma be specified and reproduced, within reasonable tolerances. The defining characteristics of the Quizapu dacite magma are:

(1) Major phase assemblage of plagioclase + amphibole + orthopyroxene, with minor magnetite + ilmenite + apatite + clinopyroxene + Fe sulfides, and absence of biotite;

(2) Plagioclase composition of An_{25-30};

(3) Melt composition reflective of the total reactive assemblage, as measured by the microlite-free glass in pumice VQ-07-37D.

In assessing experimental matches to these features, some leniency is granted in two general cases, both of which are common in phase equilibrium studies. First, minor phases (<1 vol.%) are not always encountered in thin section due to their low abundance. Second, slow reaction kinetics allow some metastable phases to persist, especially near phase boundaries. Based on the above criteria and caveats, our experimental suite at fO_2 ~NNO+0.2 indicates pre-eruptive storage of the Quizapu dacite magma, assuming $P = P_{H2O}$, at approximately 865±10 °C and 110±20 MPa (Figure 13).

(1) Phase assemblage

Several phases are present in all or a large majority of experiments, making them necessary but only broad constraints on the equilibrium conditions. Plagioclase is stable in all but the two highest pressure-temperature experiments, magnetite is stable in all but one, and apatite is stable in all runs. Ilmenite is stable in all but six experiments. Low-Ca pyroxene is present in all experiments outside the biotite stability field. Fe sulfides are almost absent, probably because no S was added to experiments to replace S entering the gas phase, or because of S reacting with the Ag sample container to form AgS grains. Thus, we do not consider the absence of Fe sulfides to invalidate conclusions about pre-eruptive storage.

The best phase assemblage constraints result from the stability curves of the two hydrous minerals. Amphibole is stable in the Quizapu magma down to relatively low pressures (~70 MPa at 830 °C), with a thermal stability limit of ~910 °C. Biotite has a lower and more abrupt temperature limit, ~855 °C, and a low-pressure limit of ~80 MPa. The lack of biotite in any erupted

Downloaded from https://academic.oup.com/petrology/advance-article/doi/10.1093/petrology/egab027/6188641 by University of Nevada at Reno user on 31 March 2021

Quizapu samples places a distinct limit on long-term storage conditions, as the magma had to be at a temperature above and/or pressure below the biotite-in curve (Figure 13), but within the amphibole stability field. Applying these criteria, the long-term dacite storage region is somewhat shallower (~110 MPa) than modeled using amphibole barometry (~130 MPa; Ruprecht *et al.*, 2012 using Ridolfi & Renzulli, 2012). Plagioclase-hornblende thermobarometry yields a similar result, peaking at 130 MPa (Figure S14; method in Anderson *et al.*, 2008 using Holland & Blundy, 1994 and Anderson & Smith, 1995). The high alkali content of the Quizapu magma ($Na_2O + K_2O = 8.4$ wt.%) favors the crystallization of mineral phases with higher alkali contents, such as amphibole (Tomiya *et al.*, 2010). Variation in the alkali content of a magma can even have a strong effect on the speciation and bonding of water in the melt (Le Losq *et al.*, 2015), which in turn are tied to amphibole stability. Thus, the high alkali content of the Quizapu magma could plausibly stabilize amphibole beyond the pressure limits calculated via barometry. The mismatch (Figure S1) between Quizapu amphiboles (Ruprecht *et al.*, 2012) and those in the calibration set (Ridolfi & Renzulli, 2012), especially in Al and Cl, is another explanation for the slightly higher barometry pressures.

(2) Plagioclase composition

The end-member dacite studied here is the most evolved magma present in the Quizapu system, with the exception of rare rhyodacite in the Plinian fall deposit (Hildreth & Drake, 1992). Given that this rhyodacite is volumetrically minor (<0.05 vol.% of the deposit) and contains only 4-5 wt.% plagioclase (Hildreth & Drake, 1992), contamination of the dacite plagioclase population by rhyodacite-derived crystals is highly unlikely. Thus, we consider the most sodic plagioclase in natural dacite samples to represent the plagioclase in equilibrium with the main dacite body. Over an extensive suite of Quizapu samples, from both 1846-1847 and 1932, the most sodic plagioclase is consistently An_{25-30} (Ruprecht *et al.*, 2012), so this range is taken to represent the stable plagioclase composition of the pre-eruptive magma chamber. Similarly, we use the most sodic experimental plagioclase compositions to draw An isopleths on Figure 13. Newly formed plagioclase is more difficult to identify in microlite-free experiments (Figure 6f); thus, we have not delineated isopleths higher than An_{35}, which would be outside the bounds of the natural match conditions.

The presence or absence of plagioclase microlites provides an independent constraint on magmatic storage conditions. For a plagioclase-bearing magma residing at equilibrium, there is no thermodynamic driving force for crystallization or resorption of the equilibrium plagioclase. At

Downloaded from https://academic.oup.com/petrology/advance-article/doi/10.1093/petrology/egab027/6188641 by University of Nevada at Reno user on 31 March 2021

temperatures and pressures below the equilibrium plagioclase isopleth, an effective undercooling (-ΔT) is induced, driving nucleation and growth of plagioclase. At temperatures and pressures above the equilibrium plagioclase isopleth, an effective superheating (+ΔT) is induced, driving resorption of plagioclase of the equilibrium composition. This thermodynamic argument is consistent with observations that plagioclase more calcic than the equilibrium composition tends to grow rims of equilibrium composition (i.e., more sodic) plagioclase, whereas plagioclase more sodic than the equilibrium composition tends to dissolve (Tsuchiyama, 1985). Experiments QZ111A and QZ111B represent a clear example of this phenomenon. These samples were run simultaneously at 850 °C and 150 MPa, but each started with material that had been previously run at different conditions – lower temperature and pressure in the case of QZ111A versus higher temperature and pressure in the case of QZ111B (Table 2). There are no plagioclase microlites in QZ111A, but some did crystallize in QZ111B (Figure S15). Thus, crystallization of microlites is expected for experiments using pumice as a starting material, at experimental conditions undercooled with respect to the storage conditions of the Quizapu dacite. Conversely, experiments that are superheated with respect to the natural equilibrium conditions should not crystallize plagioclase microlites. Consistent with glass and plagioclase compositional constraints, the band dividing microlite-bearing from microlite-free experiments passes through the region between amphibole- and biotite- in curves at 855-875 °C (Figure 6f; Figure 13), pointing to equilibrium storage at or near these conditions, which overlap the estimated storage temperature from Ruprecht & Bachmann (2010; 870 °C).

Downloaded from https://academic.oup.com/petrology/advance-article/doi/10.1093/petrology/egab027/6188641 by University of Nevada at Reno user on 31 March 2021

(3) Melt composition

Melt composition is an excellent global, albeit non-unique, representation of the state of a magmatic system. The composition of the melt depends on which crystalline phases are growing or dissolving and on their specific compositions, which in turn depend on intrinsic variables (e.g., pressure, temperature, fO_2). Diffusion of elements occurs rapidly in melt relative to silicate crystals (e.g., Zhang, 2010), meaning that melt composition is less subject to, though not free from, the kinetic limitations inherent to most crystals. Therefore, we use the melt compositions in our experimental set (as represented by quenched glasses) as thermobarometers to estimate Quizapu equilibrium storage conditions.

We arrived at the pressure-temperature envelope shown in Figures 12 and 13 via a multi-step method that involved 59 regressions in composition-temperature and composition-pressure space, each of which was compared to the glass composition of pumice VQ-07-37D and weighted by the inverse of the uncertainty range. These calculations excluded components typically present in trace abundances: MnO, P_2O_5, and Cl. Calculations and reasoning are described in detail in the Supplementary Methods. This melt compositional match region agrees with the other phase assemblage and compositional constraints (Figure 13), further constraining magmatic storage conditions. The area where this glass compositional match and experimental isopleths of An_{25-30} coincide with the stable Quizapu phase assemblage represents the H_2O-saturated storage conditions (Figure 13).

Effect of fO_2 on the Quizapu dacite phase diagram

The suite of low fO_2 experiments (Table S1) had an intrinsic fO_2 of NNO-2, allowing for a targeted comparison with the high fO_2 set discussed above (~NNO+0.2). Key findings of the low-fO_2 set are summarized by the phase diagram in Figure 14, which is markedly different from that for higher fO_2 (Figure 13). Shifts in amphibole and biotite stability represent the primary contrasts in phase equilibrium under different oxidation states, such that both are expanded at higher fO_2. For amphibole, this high-fO_2 expansion is qualitatively consistent with experiments on andesite (Martel *et al.*, 1999). For both amphibole and biotite, the expansion is primarily to lower pressures at a given temperature. At 870 °C, the amphibole curve at high fO_2, extends to nearly 40 MPa lower than at NNO-2. Around 820 °C, the biotite stability field expands to a similar extent in pressure. Beyond 850 °C, the biotite curve is nearly vertical at higher fO_2, but slopes less steeply

http://www.petrology.oupjournals.org/

Downloaded from https://academic.oup.com/petrology/advance-article/doi/10.1093/petrology/egab027/6188641 by University of Nevada at Reno user on 31 March 2021

under low-fO_2 conditions, reaching ~10 °C higher than in the NNO+0.2 experiments. Plagioclase isopleths are more widely spaced in the high-fO_2 experiments, although the An_{25-30} isopleths of the low-fO_2 experiments fall within the An_{25-30} region defined by the high-fO_2 experiments. Some of the differences in plagioclase isopleth placement are likely due to sparse sampling in the low-fO_2 experiments. In the NNO-2 experiments, Fe-Ti oxides display striking disequilibrium textures (Figure S16) and compositions (Table S3), due to their particular sensitivity to fO_2 as manifested via changes in Fe oxidation state ($Fe^{2+/3+}$). Neither their textures nor compositions (including zoning patterns) resemble any of the Quizapu oxides in Figure 8, supporting the interpretation that the experimental NNO-2 oxide features are the result of processes unrelated to the syn- and post-eruptive processes that formed the features highlighted in Figure 8. Details of the Fe-Ti oxide response to low fO_2 will be addressed in a separate contribution.

Setting aside the Fe-Ti oxides, Fe-Mg silicate phases are most affected by this large stepwise change in fO_2, due to their structural dependence on redox-sensitive iron. At higher fO_2, the ratio of Fe^{3+} to Fe^{2+} in the melt increases, reducing the Fe^{2+} available for incorporation into crystals and driving them toward higher Mg#. Because Mg-rich end-members are generally more stable than their Fe-rich counterparts, this in some cases allows for the expansion of an entire mineral stability field (e.g., biotite, Wones and Eugster, 1965). In addition, increased Fe^{3+} in the melt likely favors minerals which can easily accommodate this trivalent cation in their structures (e.g., Martel *et al.*, 1999). Amphibole and biotite are two such minerals in the Quizapu experimental system, making their greater stability range at higher fO_2 (Figures 13-14) consistent with theoretical arguments.

With Quizapu fO_2 estimated to range from NNO+0.3 to NNO+1.1 (Ruprecht *et al.*, 2012), our high-fO_2 experimental set (~ NNO+0.2) might fall slightly below the ideal fO_2 of the Quizapu magma. Compositions of Fe-Ti oxides in three experiments within the plagioclase and glass compositional match regions (QDeq34-36) suggest this is the case. At 835 °C, 150 MPa, titanomagnetite and hemoilmenite compositions are essentially those of the starting pumice, whereas at 860 °C, 125 MPa they are slightly more Ti-rich than those in the pumice (Table S2). A shift to higher fO_2 would cause these compositions to become less Ti-rich (Ghiorso & Evans, 2008), making for a better compositional match within the otherwise-determined storage region. We reiterate that these Fe-Ti oxides are volumetrically minor, and they are the phases most drastically affected by changes in environmental fO_2 (hence their utility as oxybarometers; e.g.,

http://www.petrology.oupjournals.org/

Downloaded from https://academic.oup.com/petrology/advance-article/doi/10.1093/petrology/egab027/6188641 by University of Nevada at Reno user on 31 March 2021

Ghiorso & Evans, 2008). Even so, it would take an upward shift of only 0.24 log units fO_2 at 860 °C to align Fe-Ti oxide compositions in experiment QDeq34 with those in the starting material (based on binary endmember compositions, interpolated from Buddington & Lindsley, 1964, Figure 5). This magnitude is well within the uncertainty range of most oxybarometers and thus reiterates that the experiments at ~ NNO+0.2 are a good match to Quizapu conditions.

IMPLICATIONS

Reservoir depth and size

Assuming H_2O-saturated conditions, the Quizapu assemblage is stable at depths of ~3.5 to 4.5 km deep at 865 °C, assuming ρ = 2700 kg/m^3 (Ruprecht *et al.*, 2012; Figure 13). Given the homogeneity of erupted dacites, Ruprecht *et al.* (2012) suggest that dacitic melt at Quizapu was extracted from an andesitic mush and stored in an overlying reservoir, where crystal ages suggest that the system was tapped twice, rather than rebuilt after 1846-1847 (Ruprecht & Cooper, 2012). Thus, the existence of a large magma reservoir is likely, and the total 9-10 km^3 (DRE) of material erupted over the course of the two eruptions at Quizapu provides an absolute minimum size. Recent models of the Quizapu eruptions use a chamber size of 50 km^3 (Degruyter *et al.*, 2017), based on theoretical constraints that a gas-bearing magmatic system requires ~1-10 vol.% of the chamber to be removed in any single eruption in order to return to lithostatic pressure (Bower & Woods, 1997). A perfectly spherical magma chamber in the range of 10-50 km^3 would have a radius of 1.3-2.3 km. Centered at 4 km depth, the chamber would come within 2-3 km of the surface. Activity in a shallow reservoir is consistent with the opening of a phreatic crater on nearby Descabezado Grande volcano (Figure 15) in the weeks following the climactic 1932 eruption at Quizapu (Hildreth & Drake, 1992). While there are no geophysical constraints on the magmatic plumbing system, the occurrence of Holocene mafic centers, some within 7 km of Quizapu crater (Figure 1; Hildreth & Drake, 1992; Ruprecht *et al*., 2012; Salas *et al*., 2017), argues against a much larger lateral extent of the dacite magma system, as does the mafic scoria erupted in the waning stages of the 1932 eruption, which was apparently able to penetrate through or alongside the dacite (Hildreth & Drake, 1992). Of course, the spherical chamber is a simplification, and a taller, less laterally extensive magma reservoir, possibly trending with the general NNE tectonic fabric of the region, would be consistent with both Quizapu's lateral proximity to diverse volcanic centers and with geophysical interpretations of arc magma chamber shapes (e.g. Iyer, 1984; Moran, 1994; Nagaoka *et al.*, 2012; Kiser *et al.*, 2016).

Downloaded from https://academic.oup.com/petrology/advance-article/doi/10.1093/petrology/egab027/6188641 by University of Nevada at Reno user on 31 March 2021

Our experimental setup, being H_2O-saturated, does not allow us to exclude the possibility of the Quizapu magma being undersaturated with respect to a water-rich fluid phase. However, there are as of yet no definitive constraints (*e.g.*, data on melt inclusion volatile contents, fumarole gas geochemistry) for the composition of a Quizapu magmatic volatile phase. Below we entertain the possibility of a magmatic gas phase that includes components other than H_2O, for example due to CO_2 flushing from deeper magma (e.g., Caricchi *et al.*, 2018). Based on studies of other dacite magmas, plagioclase An content increases both with X_{H2O}^{fluid} at a given P_{total} and with P_{total} at a given X_{H2O}^{fluid} (e.g., Rutherford & Devine, 1988; Hammer *et al.*, 2002). Therefore, to maintain plagioclase of $An_{25\text{-}30}$, if $X_{H2O}^{fluid} < 1$ then P_{total} must be higher than P_{H2O} of the H_2O-saturated storage region (Figure 13).

The presence of amphibole in the Quizapu assemblage suggests a possible lower bound on X_{H2O}^{fluid}, as experiments on similar dacites show that amphibole is stable when $X_{H2O}^{fluid} > \sim 0.7$ (Rutherford *et al*., 1985; Riker *et al.*, 2015). Keeping melt H_2O content equal to the saturation value at 110 MPa, a volatile phase with $X_{H2O}^{fluid} = 0.7$ corresponds to $P_{total} = 167$ MPa (Figure S17), giving an estimated maximum chamber depth of 6.3 km. Perhaps a more likely scenario is that geobarometry calculations of ~130 MPa are accurate (Ruprecht *et al.* 2012; this study Figure S14). In this case, our work demonstrates that Quizapu dacite magma residing at $P_{total} = 130$ MPa (4.9 km depth) would be H_2O undersaturated, with $X_{H2O}^{fluid} = 0.87$ (Figure S17).

Regardless of the theoretical possibilities, we emphasize that the good reproduction of the Quizapu dacite phase assemblage and compositions at $X_{H2O}^{fluid} = 1$ shows that the magma could reasonably have been stored at the H_2O-saturated conditions determined here (~ 4 km depth, Figure 13). Furthermore, using these temperatures and pressures of long-term storage, plagioclase-liquid hygrometry using the VQ-07-37D glass and $An_{25\text{-}30}$ plagioclase yields melt H_2O contents of 3.6–4.2 wt.% (standard error estimate 0.35 wt.%; Waters & Lange, 2015), consistent with calculated H_2O saturation values of 3.6–4.8 wt.% H_2O (2σ error 0.68 wt.%; Zhang *et al.*, 2007).

Refinements to the pre-eruptive heating hypothesis

In this section, we combine observations from our experiments with both new and previously reported observations of the Quizapu lavas and pyroclasts, to re-examine the prevailing hypothesis regarding the cause of the effusive nature of the 1846-1847 eruption at Quizapu (pre-eruptive heating; Ruprecht & Bachmann, 2010). We focus through the lens of the end-member dacite VQ-06-06, examining evidence to support or refute the idea that it was heated, despite no

http://www.petrology.oupjournals.org/

Downloaded from https://academic.oup.com/petrology/advance-article/doi/10.1093/petrology/egab027/6188641 by University of Nevada at Reno user on 31 March 2021

macroscopic evidence of interaction with a hotter, more mafic magma. First, we refute the notion that plagioclase microlites in the Quizapu end-member dacite are derived from the recharge andesite. Next, we discuss the heterogeneity of lava flows in terms of Fe-Ti oxide temperature. Finally, we interpret the previously unrecognized reverse zoning of orthopyroxene and develop its implications for magmatic processes. Overall, our analysis supports pre-eruptive heating prior to 1846, but introduces several important refinements to its influence in the eruption process.

The heterogeneity of the 1846-1847 lava flows is a source of some uncertainty regarding pre- and syn-eruptive magma dynamics. Some flows consist mainly of end-member dacite, such as the one from which lava VQ-06-06 was collected (Figure 1), but others consist of up to 45% mafic material in the form of enclaves (Ruprecht & Bachmann, 2010). Still others appear to represent a hybridized dacite+andesite magma. Overall, mafic material is estimated to compose 10-24 vol.% of the flow field (Ruprecht & Bachmann, 2010). The andesite involved is shown to be significantly hotter than the dacite (1050-1100 °C) via Fe-Ti oxide thermometry in enclaves (Ruprecht & Bachmann, 2010). Clearly, there is macro-scale visual evidence for variable degrees of involvement of the hotter andesite magma in the effusively erupted field. Diffusion of heat can occur more rapidly than diffusion of chemical components, however, meaning that magma which did not interact directly with the more mafic recharge may nonetheless have undergone a heating event. If the effusive eruption style was caused entirely by heating, the end-member dacite lava VQ-06-06 should represent this type of "heated only" magma.

Plagioclase microlites are present in some 1846-1847 lava flow samples, but none of the 1932 pumices. Using semi-quantitative BSE images, Ruprecht *et al.* (2012) estimate compositions of An_{30-60} for these microlites and assert that they were transferred from the recharge andesite to the resident dacite magma prior to eruption. This microlite transfer, and the idea that the dacite magma did not crystallize microlites *in situ*, has been cited as a line of evidence for heating of the dacite magma shortly prior to the 1846-1847 eruption (Ruprecht *et al.*, 2012; Ruprecht & Bachmann, 2010). Our quantitative EPMA of plagioclase microlites permits partial testing of this assertion. In the case of the dacite end-member lava VQ-06-06, the microlites span a range of anorthite content up to ~An_{40}, but cluster near An_{20} (Table S2). This range is consistent with the composition of plagioclase crystallized in our experimental samples, and feldspar microlites formed during decompression tend to be even more anorthite-rich than the equilibrium composition (Brugger & Hammer, 2010). Thus, the microlite population in dacite lava VQ-06-06

Downloaded from https://academic.oup.com/petrology/advance-article/doi/10.1093/petrology/egab027/6188641 by University of Nevada at Reno user on 31 March 2021

is consistent with *in situ* crystallization, and does not constitute evidence of syn-ascent heating. While this analysis cannot preclude some microlite transfer for strongly mingled lavas, we suggest that determining microlite compositions across a range of lava compositions is necessary for a more complete analysis of late-stage magmatic processes, including ascent, mixing, and hybridization.

However, the presence of dacite-derived microlites in and of itself does not preclude pre-eruptive heating of the magma. Even if the dacite magma is heated by recharge magma to ~1000 °C during ascent, plagioclase crystallization is thermodynamically favored at pressures below ~50 MPa (based on extrapolations of Figure 13 and of plagioclase compositional contours calculated via Waters & Lange, 2015). Thus, microlite crystallization, though potentially delayed, would not necessarily be inhibited upon ascent and eruption, even were dacites maximally heated. However, reheating to this extent at higher pressure (i.e., in the magma chamber; Ruprecht & Bachmann, 2010) would drive substantial resorption of plagioclase phenocrysts. While minor resorption of plagioclase phenocryst rims is noted in some samples (Ruprecht & Bachmann, 2010), it is not pervasive, which argues against extensive heating of the end-member dacite at depth. Therefore, if heating of the end-member dacite occurred, it was likely during magma ascent, and thus short-lived, consistent with published estimates on the order of days to weeks (Ruprecht & Cooper, 2012).

The rapidity of diffusive equilibration of Fe-Ti oxides relative to other magmatic minerals (e.g., Venezky & Rutherford, 1999) means these phases have the potential to record such late-stage events. Published estimates of Quizapu end-member dacite temperatures based on Fe-Ti oxide thermometry span a large range (837-956 °C; Hildreth & Drake, 1992; Ruprecht & Bachmann, 2010; Ruprecht *et al.*, 2012), despite evidence that long-term dacite storage conditions were relatively uniform, and similar, before each eruption. Our own analyses of Quizapu Fe-Ti oxides yield results within this range and slightly below (Figure 7, Table S3; after Ghiorso & Evans, 2008). High values of V and Mn in published analyses (Ruprecht *et al.*, 2012; Figure S7) resulted from the omission of peak interference corrections for Ti and Cr, but this compositional correction would only shift temperature estimates by ~5 °C (Table S3; after Ghiorso & Evans, 2008). Notably, temperature estimates for lava VQ-06-06 alone span ~100 °C (Figure 7), allowing for the possibility of thermal heterogeneities on the scale of single (though laterally extensive) flows. Pairs of oxides used are not necessarily touching, but it is recently recognized that averages

http://www.petrology.oupjournals.org/

Downloaded from https://academic.oup.com/petrology/advance-article/doi/10.1093/petrology/egab027/6188641 by University of Nevada at Reno user on 31 March 2021

of many compositional spots give a better measure of sample temperature than single-spot pairs in contact (Jolles & Lange, 2019). Especially in light of this new statistics-focused approach, additional study of Fe-Ti oxides in the Quizapu system is warranted. However, the current Fe-Ti oxide thermometry data cannot refute the hypothesis that the end-member dacite was heated prior to or during the 1846-1847 eruption.

Finally, reverse zoning of 1846-1847 orthopyroxene crystals in lava VQ-06-06, from En_{62-65} cores to En_{66-68} rims (Figure 4b-d, Figure 5) may reflect a small and/or rapid shift in magmatic environment relative to the stable pre-eruptive conditions in 1846-1847. Isolated orthopyroxene phenocrysts in the 1932 pumice are unzoned, implying that no similar shift occurred prior to this eruption. Because orthopyroxene richer in Mg is stable at higher temperatures, reverse zoning is consistent with heating. An oxidation event could also produce reverse zoning by lowering the activity of Fe^{2+} in the melt. Finally, degassing of H_2O can cause reverse zoning of orthopyroxene without invoking oxidation, possibly due to a preference of melt hydroxyl groups to complex with Mg^{2+} over Fe^{2+} (Waters & Lange, 2017). Below, we examine these three possibilities.

Orthopyroxene-liquid thermometry (Putirka, 2008) suggests that VQ-06-06 orthopyroxene rims record temperatures 4-15 °C hotter than those during core growth, depending on the exact bulk rock and quenched glass compositions used. Though within the ~30 °C thermometer error, the coherent relative sense and magnitude of zoning in multiple grains suggests that it originated in response to a change in intensive conditions, rather than a manifestation of compositional random scatter. Whether the rim composition reflects a few degrees of heating or is rather a snapshot of arrested equilibration due to a more significant heating event is unclear. However, the rate of Fe-Mg interdiffusion in orthopyroxene (D^{opx}_{Fe-Mg}) is on the order of 2×10^{-21} m^2 s^{-1} at 865 °C and an fO_2 of NNO+1 (Dohmen *et al.*, 2016), meaning that diffusion profiles of 5-20 μm (Figure 4b-d) would take hundreds to thousands of years to form, based on the scaling $D \sim L^2 t^{-1}$. Increasing the temperature to the maximal heating of ~1000 °C (Ruprecht & Bachmann, 2010) would still necessitate at least decadal timescales to account for the zoning. These timescales are too long to maintain the equilibrium 865 °C phase assemblage. Therefore, if a temperature increase caused the reverse zoning of orthopyroxene, the zoning developed by a process of crystal growth rather than diffusion. Consistent with this interpretation, growth protuberances are evident in Figure 4b-d (pink arrows). Our phase diagram (Figure 13) also shows that increasing temperature from the

http://www.petrology.oupjournals.org/

Downloaded from https://academic.oup.com/petrology/advance-article/doi/10.1093/petrology/egab027/6188641 by University of Nevada at Reno user on 31 March 2021

pre-eruptive storage region pushes orthopyroxene farther into its stability field, allowing for growth upon heating.

The observed change in orthopyroxene composition from core to rim could be acquired if the magma, originally stored at an fO_2 of NNO to NNO+1, experienced an oxidation event that increased the fO_2 to NNO+3.6, as calculated using the Fe speciation and fO_2 relationships of Kilinc *et al.* (1983). Assuming a constant Fe^{2+}-Mg exchange coefficient based on equilibrium between orthopyroxene cores and bulk VQ-06-06 ($Kd^{opx-liq}_{Fe^{2+}-Mg} = 0.39$), the late-stage melt, represented by the average pumice glass composition of VQ-07-37D, would require a molar Fe^{3+}/Fe^{total} of 0.59, compared to the initial value of 0.26, in order to crystallize the observed orthopyroxene rims. Using the VQ-06-06 residual glass composition instead increases the required Fe^{3+}/Fe^{total} ratio of the melt to 0.78, corresponding to an fO_2 of NNO+5.5, roughly 1.3 log units above the magnetite-hematite transition (Zolotov & Fegley, 1999). An fO_2 of ~NNO+2 or higher would cross the stability bound of magmatic sulfides (Jugo, 2009; Carroll & Rutherford, 1985), and thus be consistent with the breakdown of Fe-S globules in VQ-06-06 (Figure 8d). However, there is no evidence of magnetite destabilization, suggesting the fO_2 remained below ~NNO+4.2. Oxidation is most commonly attributed to magma degassing on ascent, although it requires components beyond pure H_2O (e.g., Cl-bearing fluids, Bell & Simon, 2011; S-bearing fluids; Burgisser & Scaillet, 2007), as recent work on silicic magmas demonstrates that degassing of H_2O alone cannot cause melt oxidation (Waters and Lange, 2016). However, experiments on Fe scavenging by Cl-bearing volatile phases in arc magmas show a maximum increase of ~1.5 log units fO_2 due to this process (Bell & Simon, 2011). Thus, with no evidence of crustal assimilation or other mechanisms of oxidation beyond degassing, it is unlikely that oxidation alone would have been extreme enough to cause the formation higher-Mg rims on orthopyroxene. Additionally, this study shows that oxidation expands the biotite stability field at the expense of orthopyroxene (Figure 13, Figure 14).

Although H_2O degassing would not cause oxidation of the magma, experiments demonstrate that equilibrium orthopyroxene compositions are more Fe-rich at higher H_2O contents, irrespective of temperature and pressure, due to a hypothesized preference of melt hydroxyl groups to complex with Mg^{2+} over Fe^{2+} (Waters & Lange, 2017); thus, degassing of H_2O from the melt can result in the growth of progressively more magnesian orthopyroxene. The observed $Kd^{opx-liq}_{Fe^{2+}-Mg}$ values for orthopyroxene cores in equilibrium with VQ-06-06 bulk rock (0.39) and rims in equilibrium with VQ-06-06 or VQ-07-37D residual glass (0.12-0.22) are

http://www.petrology.oupjournals.org/

Downloaded from https://academic.oup.com/petrology/advance-article/doi/10.1093/petrology/egab027/6188641 by University of Nevada at Reno user on 31 March 2021

consistent with melt H_2O contents of 4.1 wt.% H_2O and 0.3-1.8 wt.% H_2O, respectively (Waters & Lange, 2017; regression on Figure 4D). An H_2O content of 4.1 wt.% for the Quizapu dacite matches the storage conditions determined here (Figure 13), as well as hygrometer estimates (Ruprecht *et al.*, 2012). The lower H_2O contents implied by the $Kd_{Fe^{2+}-Mg}^{opx-liq}$ of orthopyroxene rims are consistent with decreasing melt H_2O content during ascent and degassing of the magma.

We have presented several explanations for reverse zoning in VQ-06-06 orthopyroxene crystals. Though we cannot definitively ascribe the higher-Mg rims to one process, the above calculations combined with the experimentally-determined phase diagrams suggest that 4-15 °C of heating, or degassing of 2.3-3.8 wt.% H_2O are the best explanations for the observed difference in composition. A combination of heating and degassing is also consistent with the current pre-eruptive model, as H_2O solubility decreases with increasing temperature, and eventual widespread and passive outgassing is a requirement for the effusive nature of the eruption.

The orthopyroxene crystals in the 1932 pumice are unzoned and match the composition of the VQ-06-06 orthopyroxene rims (Figure 4a, Figure 5). Given the otherwise close to identical phase assemblage of the 1846-1847 and 1932 dacites, this observation is consistent with a relatively small shift in conditions that persisted between eruptions, unresolvable within the experimental spacing in this study. A temperature increase on the order of 10 °C would have far less consequence for the phase assemblage than a decrease in melt H_2O content of ~3 wt.% (Figure 13), and this subtly different thermal state could conceivably be maintained for 86 years in a chamber of relatively large volume and compact shape. Thus, the demonstrable involvement of a hotter, mafic magma in the overall 1846-1847 eruption remains a robust and simple mechanism for inducing both the larger suite of variation in the 1846-1847 minerals across the flow field and the subtle higher-Mg rims in VQ-06-06 orthopyroxene that match homogeneous 1932 crystals.

These features of orthopyroxene are complemented by incipient, fine-scale destabilization of some amphibole crystals in the same sample, VQ-06-06. Upon close inspection, some of the "stable, euhedral" amphibole crystals (Figure 16a) display micron-scale dissolution textures and are surrounded in part by plagioclase and bright phases that are likely Fe-Ti oxides and/or pyroxene crystals too small for quantitative analysis (Figure 16b). Viewed through the lens of our experimentally-determined phase diagrams, an oxidation event (already ruled out as the sole cause of higher-Mg orthopyroxene rims) would drive amphibole further into its stability field, which is inconsistent with the evidence of incipient amphibole dissolution. On the other hand, a decrease

Downloaded from https://academic.oup.com/petrology/advance-article/doi/10.1093/petrology/egab027/6188641 by University of Nevada at Reno user on 31 March 2021

of ~3 wt.% H_2O upon degassing would push amphibole far outside its stability region. However, the kinetics of amphibole breakdown could preclude an immediate response (e.g., Hammer & Rutherford, 2003). Finally, a heating event, even of 10 °C, brings amphibole near its stability bound, whereas low-Ca pyroxene moves deeper into its region of stability (Figure 13). Thus, a heating origin can explain both the higher-Mg orthopyroxene rims and the destabilization of amphibole. The proximity to the amphibole-out curve also means that incremental shifts in pressure or H_2O content would still allow amphibole to persist in the 1932 dacite.

Controls on eruptive style

Despite the clear involvement of andesite recharge in some parts of the Quizapu flow field, there is no unambiguous evidence that the end-member dacite was heated more than ~10 °C degrees above its equilibrium storage temperature in 1846-1847. If viscosity decrease effected by heating was the cause for effusive eruption, then how did multiple flow lobes with end-member dacite erupt with little to no evidence of heating? Given the effusive style of the 1846-1847 eruption, regardless of flow-scale evidence of heating, we conclude that heating was unlikely to have been the only influence on eruptive style. If heating was not the sole difference between the effusive 1846-1847 eruption and the explosive 1932 eruption, then what additional parameters controlled the eruptive styles?

The near-identical nature of the 1846-1847 and 1932 end-member dacites suggested from the start that long-term storage conditions did not influence eruptive style at Quizapu. Although we did not vary X_{H2O}^{fluid}, H_2O-saturated conditions successfully reproduced the phase assemblage from both eruptions, and the presence of stable amphibole in both cases suggests that long-term melt volatile content and storage temperatures were not appreciably different in 1846-1847 than in 1932. However, thermomechanical modeling of the Quizapu eruptions suggests that, while maintaining melt volatile saturation, the presence or absence of a free fluid phase could explain the difference in eruptive styles (Degruyter et al., 2017). An exsolved volatile phase prior to the 1846-1847 eruption would dampen pressure buildup due to magma recharge, creating a feedback allowing for a large volume of recharge magma to impart heat prior to eruption. Associated pressure-induced dissolution of H_2O would have been exothermic, releasing heat that increased the temperature of the dacite further. After passive outgassing and effusive eruption, the magma could have been left without a gas phase, leaving no pressurization buffer prior to the 1932 Plinian eruption. This Degruyter *et al.* model has intriguing potential; however, the putative reheating

Downloaded from https://academic.oup.com/petrology/advance-article/doi/10.1093/petrology/egab027/6188641 by University of Nevada at Reno user on 31 March 2021

process would have to have been very restricted in time. While extended priming of the magma system by recharge over decades, as modeled by Degruyter et al. (2017), may be generally consistent with enclave accumulation and survival during prolonged recharge (Ruprecht *et al*., 2020), it would decrease the overall magma crystallinity and change mineral textures (e.g., extensive amphibole breakdown, resorption of An_{25-30} plagioclase) in a manner that is inconsistent with the observations from 1846-1847 dacite end-member lavas. Nonetheless, a heterogeneous distribution of exsolved volatiles prior to the 1846-1847 eruption would help explain the flow-field heterogeneity and mixed petrographic evidence of heating, since areas with greater volatile resorption would be subject to greater heating. Given that H_2O has a heat capacity ~2.6 times higher than CO_2 at magmatic conditions (3.5568 J g^{-1} K^{-1} versus 1.3587 J g^{-1} K^{-1} at 110 MPa, 825 °C; Lemon et al., 1997), a mixed volatile phase with lower X_{H2O}^{fluid} due to the presence of CO_2 would be less able to thermally buffer the dacite magma from an influx of hotter recharge magma. Thus, heterogeneities in X_{H2O}^{fluid} could produce similar effects without invoking the entire appearance or disappearance of a free volatile phase. The presence and composition of exsolved magmatic volatiles, and their spatial distribution in the magma reservoir, may be key parameters to explore in future studies.

Along with this heat-amplification model, we can turn toward other processes within the sub-volcanic plumbing system to help explain the eruption style changes. The 1846-1847 magma may have outgassed prior to extrusion due to the formation of a permeable foam (Eichelberger *et al.*, 1986), or more gradual gas loss due to strain-induced outgassing via permeable pathways (e.g. Caricchi *et al.*, 2011) or melt fracturing (e.g. Gonnermann & Manga, 2003; Cabrera *et al.*, 2015). Relatively slow ascent rate is necessary to allow for sufficient outgassing, by whichever means it occurs, and is evidenced by the duration of the Quizapu effusive eruption, which lasted ~100 times longer than the 1932 Plinian eruption while expelling the same volume (DRE) of material. Yet, ascent rates need to be fast enough to limit amphibole breakdown (e.g., Rutherford, 2008). One key to allowing slow ascent, and thereby sufficient outgassing to preclude explosive eruption, may lie in conduit processes or geometry. Equally important may be the fact that amphibole stability for the Quizapu dacite extends to significantly lower pressures than for compositions where amphibole breakdown was experimentally studied (Rutherford & Hill,1993; Brown & Gardner, 2006; De Angelis *et al.*, 2015). This means that amphibole rim development in ascending Quizapu magma could have been delayed, possibly even prevented, for an extended part of the ascent.

http://www.petrology.oupjournals.org/

Downloaded from https://academic.oup.com/petrology/advance-article/doi/10.1093/petrology/egab027/6188641 by University of Nevada at Reno user on 31 March 2021

There is evidence that some silicic lava flows and domes erupt along fissures, at least initially, rather than issuing from central vents (e.g. Medicine Lake, Donnelly-Nolan *et al.*, 2016), and Quizapu appears to follow this trend. Hildreth & Drake (1992) interpret the observations of eye witnesses and early post-eruption reports to indicate that the eruptive vent for the 1846-1847 eruption was most likely a ~1 km long fissure, trending NNE. This geometry is also consistent with the wide flow field near the vent area and individual flows projecting to various extrusion locations rather than a single point source. Fissures can accommodate high discharge rates at relatively slow ascent rates, compared to point source vents, where an equally high discharge rate would correspond to far more rapid ascent. A fissure geometry also provides greater surface area over which magma is in contact with wall rock or atmosphere, allowing outgassing at higher rates, which favors effusive eruption. Pre-existing fractures in the upper crust allow for easy fissure formation in certain locations, a critical element that allows the resultant eruption to have an effusive rather than explosive character, given the same initial magma pressure and volatile content (e.g. Yellowstone, Loewen *et al.*, 2017). There is abundant evidence for pre-existing crustal structures in the Andes, from major fault zones to smaller compressional structures that strike roughly along-arc in a NNE direction and define many volcanic clusters (Cembrano & Lara, 2009). Mafic volcanic centers, not expected given the 45-km thick crust, occur in the Southern Volcanic Zone due to facilitated magma ascent through crustal structures related to the Andean arc and even pre-Andean tectonic regimes (Salas *et al.*, 2017). It is thus reasonable to expect that some of these same or similar structures may influence the more prevalent, silicic volcanism in the region.

The hypothesized NNE-trending fissure vent at Quizapu would roughly align with the arc itself, and more locally, with the Cerro Azul-Descabezado Grande volcanic axis (Figure 1), making it consistent with the regional tectonic trends. The cessation of the 1846-1847 eruption appears to have left unerupted material to solidify in the vent, which is partially visible in the current crater wall (Hildreth & Drake, 1992, their Figures 5-6). This massive, un-brecciated filling of the eruptive fissure would have forced magma to take a different path to the surface in 1932, and, lacking access to another easily-opened fissure, it discharged through a point source vent in a highly explosive eruption.

Further work to establish the eruptive sequence of the extruded lava flows, thus far inconclusive (Hildreth & Drake, 1992; Ruprecht *et al.*, 2012; Higgins *et al.*, 2015), is needed, along with a dedicated effort to establish if any lavas came from vents not coincident with the

http://www.petrology.oupjournals.org/

Downloaded from https://academic.oup.com/petrology/advance-article/doi/10.1093/petrology/egab027/6188641 by University of Nevada at Reno user on 31 March 2021

current Quizapu crater, and if so, whether those sources were fissures, and how long they might have been. With extensive field work already undertaken, creative approaches are needed, for example, a combination of aerial observations, geophysical work, and additional petrologic studies. For example, reaction rims on amphibole crystals in mingled and hybridized lobes could result from variable ascent rates, a temperature change, or both (e.g. Rutherford & Hill, 1993; DeAngelis *et al.*, 2015). Careful analysis of these rims and mapping of their occurrence (and the occurrence of pristine amphibole) may provide further insight. Although heating is not the sole driver of eruptive style for the flow field, it likely played a large role in some portions of the field, and at particular points in the temporal sequence of the eruption. The interplay of this dynamic event with pre-existing volatile phases, conduit geometry, and ascent processes, is a promising new avenue of study.

CONCLUSIONS

Assuming H_2O-saturated conditions, the Quizapu dacite equilibrated at 865±10 °C and 110±20 MPa (4 km), based on laboratory experiments defining fields of stability of the major phase assemblage: $An_{25\text{-}30}$ plagioclase + amphibole + orthopyroxene + glass. Within the resolution of our methods, these conditions apply to magmatic storage before both the 1846-1847 and 1932 eruptions, despite evidence that the system may have thermally equilibrated to a slightly higher temperature following mafic recharge prior to the 1846-1847 eruption. An fO_2 decrease in the Quizapu bulk compositional space restricts the stability fields of biotite and amphibole to higher pressures and lower temperatures. Though not observed for Quizapu, such a change in fO_2 is likely to have similar effects in other dacite systems, and could plausibly result from an influx of more reduced, mafic magma. These experimental insights were informed by careful petrographic and compositional study of natural dacite samples, which led to further refinement of the complex dynamics at work in the unusual effusive-then-explosive Quizapu eruptions. Future volcanic crises are almost certain to occur, given the active nature of the Cerro Azul-Descabezado Grande volcanic axis. Our work paves the way for a deeper understanding of the Quizapu system and lays out key comparison points for modeling past or future departures from equilibrium.

Downloaded from https://academic.oup.com/petrology/advance-article/doi/10.1093/petrology/egab027/6188641 by University of Nevada at Reno user on 31 March 2021

DATA AVAILABILITY

The data underlying this article are available in the article and in its online supplementary material. Should any additional information or alternate formats of data be desired, we encourage readers to contact the authors, who will be happy to provide the requested material.

FUNDING

This work was supported by the National Science Foundation [EAR 1347887 to J.E.H., EAR 1347880/1717288 to P.R.] and the Columbia President's Global Innovation Fund [to P.R.].

ACKNOWLEDGEMENTS

We are grateful to Eric Hellebrand and Joe Boesenberg for their EPMA analytical expertise, JoAnn Sinton for making thin sections of the Quizapu lava and pumice, and Diamond Tachera for acquiring transmitted light images and point counting the VQ-06-06 lava. Roy Tom provided exceptional machining work, and Carrie Brugger-Schorr collected the pumice sample. Kelsey Prissel went above and beyond to run the new FeTi Oxide Geotherm app for us. We thank Tom Shea, Bruce Houghton, and Benoît Welsch for comments on various versions of the manuscript. Fidel Costa prompted a closer look at Volcán San Pedro. We appreciate reviews by J. Blundy, L. Waters, and an anonymous reviewer that led us to perform additional experiments that greatly improved this contribution. We thank J. Blundy, C. Martel, and another anonymous reviewer for comments on the final submission. E.C.F. and J.H. attended a workshop and field excursion to Quizapu in February 2016, led by P.R. and aided greatly by the local arrieros and their trusty horses. E.C.F. is grateful to the ARCS Foundation Honolulu chapter for additional support. This work is part of the PhD dissertation of E.C.F. and is SOEST publication #XXXX.

REFERENCES

Anderson, J. L., Barth, A. P., Wooden, J. L. & Mazdab, F. (2008). Thermometers and Thermobarometers in Granitic Systems. *Reviews in Mineralogy and Geochemistry* **69**, 121–142.

Anderson, J. L. & Smith, D. R. (1995). The effects of temperature and f_{O2} on the Al-in-hornblende barometer. *American Mineralogist* **80**, 549–559.

Andújar, J. & Scaillet, B. (2012). Relationships between pre-eruptive conditions and eruptive styles of phonolite–trachyte magmas. *Lithos* **152**, 122–131.

Armstrong, J. T. (1988). Quantitative analysis of silicate and oxide materials: Comparison of Monte Carlo, ZAF, and $\phi(\rho z)$ procedures. In: Newbury, D. E. (ed.) *Microbeam Analysis*

Downloaded from https://academic.oup.com/petrology/advance-article/doi/10.1093/petrology/egab027/6188641 by University of Nevada at Reno user on 31 March 2021

1988: Proceedings of the 23rd Annual Conference of the Microbeam Analysis Society, Milwaukee, Wisconsin, 8-12 August 1988. San Francisco: San Francisco Press, 239-246.

Bachmann, O. & Dungan, M. A. (2002). Temperature-induced Al-zoning in hornblendes of the Fish Canyon magma, Colorado. *American Mineralogist* **87**, 1062–1076.

Bacon, C. R. & Hirschmann, M. M. (1988). Mg/Mn partitioning as a test for equilibrium between coexisting Fe-Ti oxides. *American Mineralogist* **73**, 57–61.

Bell, A. S. & Simon, A. (2011). Experimental evidence for the alteration of the Fe3+/ΣFe of silicate melt caused by the degassing of chlorine-bearing aqueous volatiles. *Geology* **39**, 499–502.

Bower, S. M. & Woods, A. W. (1997). Control of magma volatile content and chamber depth on the mass erupted during explosive volcanic eruptions. *Journal of Geophysical Research* **102**, 10273–10290.

Browne, B. & Gardner, J. (2006). The influence of magma ascent path on the texture, mineralogy, and formation of hornblende reaction rims. *Earth and Planetary Science Letters* **246**, 161–176.

Brugger, C. R. & Hammer, J. E. (2010). Crystallization Kinetics in Continuous Decompression Experiments: Implications for Interpreting Natural Magma Ascent Processes. *Journal of Petrology* **51**, 1941–1965.

Bryan, W. B. (1972). Morphology of quench crystals in submarine basalts. *Journal of Geophysical Research* **77**, 5812–5819.

Buddington, A. F. & Lindsley, D. H. (1964). Iron-titanium oxide minerals and synthetic equivalents. *Journal of petrology* **5**, 310–357.

Burgisser, A. & Scaillet, B. (2007). Redox evolution of a degassing magma rising to the surface. *Nature* **445**, 194–197.

Cabrera, A., Weinberg, R. F. & Wright, H. M. N. (2015). Magma Fracturing and Degassing Associated with Obsidian Formation: The Explosive-Effusive Transition. *Journal of Volcanology and Geothermal Research* **298**, 71–84.

Caricchi, L., Pommier, A., Pistone, M., Castro, J., Burgisser, A. & Perugini, D. (2011). Strain-induced magma degassing: insights from simple-shear experiments on bubble bearing melts. *Bulletin of Volcanology* **73**, 1245–1257.

Caricchi, L., Sheldrake, T. E. & Blundy, J. (2018). Modulation of magmatic processes by CO_2 flushing. *Earth and Planetary Science Letters* **491**, 160–171.

Carroll, M. R. & Rutherford, M. J. (1985). Sulfide and sulfate saturation in hydrous silicate melts. *Journal of Geophysical Research* **90**, C601.

Castro, J. M., Schipper, C. I., Mueller, S. P., Militzer, A. S., Amigo, A., Parejas, C. S. & Jacob, D. (2013). Storage and eruption of near-liquidus rhyolite magma at Cordón Caulle, Chile. *Bulletin of Volcanology* **75**.

Cembrano, J. & Lara, L. (2009). The link between volcanism and tectonics in the southern volcanic zone of the Chilean Andes: A review. *Tectonophysics* **471**, 96–113.

Costa, F., Scaillet, B. & Pichavant, M. (2004). Petrological and Experimental Constraints on the Pre-eruption Conditions of Holocene Dacite from Volcán San Pedro (36 S, Chilean Andes) and the Importance of Sulphur in Silicic Subduction-related Magmas. *Journal of Petrology* **45**, 855–881.

Dall'Agnol, R., Scaillet, B. & Pichavant, M. (1999). An Experimental Study of a Lower Proterozoic A-type Granite from the Eastern Amazonian Craton, Brazil. *Journal of Petrology* **40**, 1673–1698.

Downloaded from https://academic.oup.com/petrology/advance-article/doi/10.1093/petrology/egab027/6188641 by University of Nevada at Reno user on 31 March 2021

De Angelis, S. H., Larsen, J., Coombs, M., Dunn, A. & Hayden, L. (2015). Amphibole reaction rims as a record of pre-eruptive magmatic heating: An experimental approach. *Earth and Planetary Science Letters* **426**, 235–245.

Degruyter, W., Huber, C., Bachmann, O., Cooper, K. M. & Kent, A. J. R. (2017). Influence of exsolved volatiles on reheating silicic magmas by recharge and consequences for eruptive style at Volcan Quizapu (Chile). *Geochemistry, Geophysics, Geosystems* **18**, 4123-4135.

Devine, J. D., Gardner, J. E., Brack, H. P., Layne, G. D., Rutherford, M. J. (1995). Comparison of microanalytical methods for estimating H_2O contents of silicic volcanic glasses. *American Mineralogist* **80**, 319-328.

Di Muro, A., Pallister, J., Villemant, B., Newhall, C., Semet, M., Martinez, M. & Mariet, C. (2008). Pre-1991 sulfur transfer between mafic injections and dacite magma in the Mt. Pinatubo reservoir. *Journal of Volcanology and Geothermal Research* **175**, 517–540.

Dohmen, R., Ter Heege, J. H., Becker, H.-W. & Chakraborty, S. (2016). Fe-Mg interdiffusion in orthopyroxene. *American Mineralogist* **101**, 2210–2221.

Donnelly-Nolan, J. M., Champion, D. E. & Grove, T. L. (2016). Late Holocene Volcanism at Medicine Lake Volcano, Northern California Cascades. *U.S. Geological Survey Professional Paper* **1822**, 59 p.

Donovan, J. J., Snyder, D. A. & Rivers, M. L. (1993). An improved interference correction for trace element analysis. *Microbeam Analysis* **2**, 23–28.

Drake, R. E. (1976). Chronology of Cenozoic igneous and tectonic events in the central Chilean Andes- Latitudes 35°30' to 36°S. *Journal of Volcanology and Geothermal Research* **1**, 265–284.

Droop, G. T. R. (1987). A general equation for estimating Fe^{3+} concentrations in ferromagnesian silicates and oxides from microprobe analyses, using stoichiometric criteria. *Mineralogical Magazine* **51**, 431–435.

Eggler, D. H. & Burnham, C. W. (1973). Crystallization and Fractionation Trends in the System Andesite-H_2O-CO_2-O_2 at Pressures to 10 Kb. *GSA Bulletin* **84**, 2517–2532.

Eichelberger, J. C., Carrigan, C. R., Westrich, H. R. & Price, R. H. (1986). Non-explosive silicic volcanism. *Nature* **323**, 598–602.

Eugster, H. P. & Skippen, B. (1967). Igneous and metamorphic reactions involving gas equilibria. In: Ableson, P. H. (ed) *Researches in Geochemistry*. New York: John Wiley and Sons, 492–520.

Faure, F., Trolliard, G., Nicollet, C. & Montel, J.-M. (2003). A developmental model of olivine morphology as a function of the cooling rate and the degree of undercooling. *Contributions to Mineralogy and Petrology* **145**, 251–263.

Fiege, A., Ruprecht, P. & Simon, A. (2017). A magma mixing redox trap that moderates mass transfer of sulphur and metals. *Geochemical Perspectives Letters* 190–199.

First, E. & Hammer, J. (2016). Igneous cooling history of olivine-phyric shergottite Yamato 980459 constrained by dynamic crystallization experiments. *Meteoritics & Planetary Science* **51**, 1233–1255.

First, E. C., Leonhardi, T. C. & Hammer, J. E. (2020). Effects of superheating magnitude on olivine growth. *Contributions to Mineralogy and Petrology* **175**, 13.

Fuenzalida, H. (1942). El Volcán Descabezado Grande. *Boletin del Museo Nacional de Historia Natural* **21**, 37–53.

Downloaded from https://academic.oup.com/petrology/advance-article/doi/10.1093/petrology/egab027/6188641 by University of Nevada at Reno user on 31 March 2021

Gardner, J. E., Rutherford, M., Carey, S. & Sigurdsson, H. (1995). Experimental constraints on pre-eruptive water contents and changing magma storage prior to explosive eruptions of Mount St. Helens volcano. *Bulletin of Volcanology* **57**, 1–17.

Geschwind, C.-H. & Rutherford, M. J. (1992). Cummingtonite and the evolution of the Mount St Helens (Washington) magma system: an experimental study. *Geology* **20**, 1011–1014.

Ghiorso, M. S. & Evans, B. W. (2008). Thermodynamics of rhombohedral oxide solid solutions and a revision of the Fe-Ti two-oxide geothermometer and oxygen-barometer. *American Journal of science* **308**, 957–1039.

Ghiorso, M. S. & Prissel, K. B. (2020). *ENKI Cloud App: Implementation of the Fe-Ti Oxide Geothermooxybarometer of Ghiorso and Evans, 2008*. Zenodo.

Gonnermann, H. M. & Manga, M. (2003). Explosive volcanism may not be an inevitable consequence of magma fragmentation. *Nature* **426**, 432–435.

Gonnermann, H. M. & Manga, M. (2012). Dynamics of magma ascent in the volcanic conduit. In: Fagents, S. A., Gregg, T. K. P. & Lopes, R. M. C. (eds) *Modeling Volcanic Processes: The Physics and Mathematics of Volcanism*. Cambridge, England: Cambridge University Press, 55–84.

Grocke, S. B., Andrews, B. J. & de Silva, S. L. (2017). Experimental and petrological constraints on long-term magma dynamics and post-climactic eruptions at the Cerro Galán caldera system, NW Argentina. *Journal of Volcanology and Geothermal Research* **347**, 296–311.

Grunder, A. & Mahood, G. (1988). Physical and Chemical-Models of Zoned Silicic Magmas - the Loma Seca Tuff and Calabozos Caldera, Southern Andes. *Journal of Petrology* **29**, 831–867.

Hammer, J. E. (2008). Experimental Studies of the Kinetics and Energetics of Magma Crystallization. *Reviews in Mineralogy and Geochemistry* **69**, 9–59.

Hammer, J., Jacob, S., Welsch, B., Hellebrand, E. & Sinton, J. (2016). Clinopyroxene in postshield Haleakala ankaramite: 1. Efficacy of thermobarometry. *Contributions to Mineralogy and Petrology* **171**:7.

Hammer, J. E., Rutherford, M. J. & Hildreth, W. (2002). Magma storage prior to the 1912 eruption at Novarupta, Alaska. *Contributions to Mineralogy and Petrology* **144**, 144–162.

Hammer, J. E. & Rutherford, M. J. (2003). Petrologic indicators of preeruption magma dynamics. *Geology* **31**, 79–82.

Higgins, M. D., Voos, S. & Vander Auwera, J. (2015). Magmatic processes under Quizapu volcano, Chile, identified from geochemical and textural studies. *Contributions to Mineralogy and Petrology* **170**:51.

Hildreth, W. & Drake, R. E. (1992). Volcán Quizapu, Chilean Andes. *Bulletin of Volcanology* **54**, 93–125.

Hildreth, W., Grunder, A. & Drake, R. (1984). The Loma Seca Tuff and the Calabozos caldera: A major ash-flow and caldera complex in the southern Andes of central Chile. *Geological Society of America Bulletin* **95**, 45–54.

Holland, T. & Blundy, J. (1994). Non-ideal interactions in calcic amphiboles and their bearing on amphibole-plagioclase thermometry. *Contributions to Mineralogy and Petrology* **116**, 433-447.

Holtz, F. (2005). Experimental Petrology of the 1991-1995 Unzen Dacite, Japan. Part I: Phase Relations, Phase Composition and Pre-eruptive Conditions. *Journal of Petrology* **46**, 319–337.

Downloaded from https://academic.oup.com/petrology/advance-article/doi/10.1093/petrology/egab027/6188641 by University of Nevada at Reno user on 31 March 2021

Houghton, B. F., Carey, R. J., Cashman, K. V., Wilson, C. J. N., Hobden, B. J. & Hammer, J. E. (2010). Diverse patterns of ascent, degassing, and eruption of rhyolite magma during the 1.8 ka Taupo eruption, New Zealand: Evidence from clast vesicularity. *Journal of Volcanology and Geothermal Research* **195**, 31–47.

Iyer, H. M. (1984). Geophysical evidence for the locations, shapes and sizes, and internal structures of magma chambers beneath regions of Quaternary volcanism. *Philosophical Transactions of the Royal Society of London A: Mathematical, Physical and Engineering Sciences* **310**, 473–510.

Jakobsson, S. & Oskarsson, N. (1994). The system C-O in equilibrium with graphite at high pressure and temperature: An experimental study. *Geochimica et Cosmochimica Acta* **58**, 9–17.

Jarosewich, E., Parkes, A. S., & Wiggins, L. B. (1979). Microprobe analyses of four natural glasses and one mineral: An interlaboratory study of precision and accuracy. *Smithsonian Contributions to the Earth Sciences* **22**, 53-67.

Jarosewich, E., Nelen, J. A. & Norberg, J. A. (1980). Reference samples for electron microprobe analysis. *Geostandards Newsletter* **IV**, 43–47.

Jochum, K. P. *et al.* (2006). MPI-DING reference glasses for in situ microanalysis: New reference values for element concentrations and isotope ratios. *Geochemistry, Geophysics, Geosystems* **7**, Q02008.

Johnson, M. C., Anderson, A. T. & Rutherford, M. J. (1994). Pre-eruptive volatile contents of magmas. *Reviews in Mineralogy and Geochemistry* **30**, 281–330.

Jolles, J. S. R. & Lange, R. A. (2019). High-resolution Fe–Ti oxide thermometry applied to single-clast pumices from the Bishop Tuff: a re-examination of compositional variations in phenocryst phases with temperature. *Contributions to Mineralogy and Petrology* **174**, 70.

Jugo, P. J. (2009). Sulfur content at sulfide saturation in oxidized magmas. *Geology* **37**, 415–418.

Kilinc, A., Carmichael, I. S. E., Rivers, M. L. & Sack, R. O. (1983). The ferric-ferrous ratio of natural silicate liquids equilibrated in air. *Contributions to Mineralogy and Petrology* **83**, 136–140.

Kiser, E., Palomeras, I., Levander, A., Zelt, C., Harder, S., Schmandt, B., Hansen, S., Creager, K. & Ulberg, C. (2016). Magma reservoirs from the upper crust to the Moho inferred from high-resolution Vp and Vs models beneath Mount St. Helens, Washington State, USA. *Geology* **44**, 411–414.

Kress, V. (1997). Magma mixing as a source for Pinatubo sulphur. *Nature* **389**, 591–593.

Lange, R. A., Frey, H. M. & Hector, J. (2009). A thermodynamic model for the plagioclase-liquid hygrometer/thermometer. *American Mineralogist* **94**, 494–506.

Larocque, A. C. L., Stimac, J. A., Keith, J. D. & Huminicki, M. A. E. (2000). Evidence for open-system behavior in immiscible Fe-S-O liquids in silicate magmas: Implications for contributions of metals and sulfur to ore-forming fluids. *The Canadian Mineralogist* **38**, 1233–1249.

Larsen, J. F. (2006). Rhyodacite magma storage conditions prior to the 3430 yBP caldera-forming eruption of Aniakchak volcano, Alaska. *Contributions to Mineralogy and Petrology* **152**, 523–540.

Lattard, D., Sauerzapf, U. & Kontny, A. (2012). Rapid surficial oxidation of synthetic Fe-Ti oxides at high temperature: Observations and consequences for magnetic measurements. *Geochemistry, Geophysics, Geosystems* **13**, Q08Z46.

Leake, B. E. (1978). Nomenclature of amphiboles. *American Mineralogist* **63**, 1023–1052.

Downloaded from https://academic.oup.com/petrology/advance-article/doi/10.1093/petrology/egab027/6188641 by University of Nevada at Reno user on 31 March 2021

Le Losq, C., Mysen, B. O., Cody, G. D., (2015). Water and magmas: Insights about the water solution mechanisms in alkali silicate melts from infrared, Ramen, and ^{29}Si solid-state NMR spectroscopies. *Progress in Earth and Planetary Science* 2:22.

Lemon, E. W., McLinden, M. O. & Friend, D. G. (1997). Thermophysical Properties of Fluid Systems. In: Linstrom, P. J. & Mallard, W. G. (eds) *NIST Chemistry WebBook, NIST Standard Reference Database Number 69*. Gaithersburg: National Institute of Standards and Technology.

Lipman, P. W. & Mullineaux, D. R. (eds) (1985). The 1980 Eruptions of Mount St. Helens, Washington. *U.S. Geological Survey Professional Paper* **1250**, 844 p.

Loewen, M. W., Bindeman, I. N. & Melnik, O. E. (2017). Eruption mechanisms and short duration of large rhyolitic lava flows of Yellowstone. *Earth and Planetary Science Letters* **458**, 80–91.

Martel, C., Pichavant, M., Holtz, F., Scaillet, B., Bourdier, J.-L. & Traineau, H. (1999). Effects of fO_2 and H_2O on andesite phase relations between 2 and 4 kbar. *Journal of Geophysical Research* **104**, 29453–29470.

Médard, E. & Grove, T. L. (2008). The effect of H_2O on the olivine liquidus of basaltic melts: experiments and thermodynamic models. *Contributions to Mineralogy and Petrology* **155**, 417–432.

Merzbacher, C. & Eggler, D. H. (1984). A magmatic geohygrometer: application to Mount St. Helens and other dacitic magmas. *Geology* **12**, 587–590.

Moore, G., Vennemann, T. & Carmichael, I. S. E. (1998). An empirical model for the solubility of H_2O in magmas to 3 kilobars. *American Mineralogist* **83**, 36–42.

Moran, S. C. (1994). Seismicity at Mount St. Helens, 1987–1992: Evidence for repressurization of an active magmatic system. *Journal of Geophysical Research: Solid Earth* **99**, 4341–4354.

Muir, D. D., Blundy, J. D., Rust, A. C. & Hickey, J. (2014). Experimental Constraints on Dacite Pre-eruptive Magma Storage Conditions beneath Uturuncu Volcano. *Journal of Petrology* **55**, 749–767.

Nagaoka, Y., Nishida, K., Aoki, Y., Takeo, M. & Ohminato, T. (2012). Seismic imaging of magma chamber beneath an active volcano. *Earth and Planetary Science Letters* **333**–**334**, 1–8.

Nakada, S., Shimizu, H. & Ohta, K. (1999). Overview of the 1990 1995 eruption at Unzen Volcano. *Journal of Volcanology and Geothermal Research* **89**, 1–22.

Nakamura, Y. (1973). Origin of sector-zoning in igneous clinopyroxenes. *American Mineralogist* **58**, 986–990.

Newhall, C. G. & Punongbayan, R. S. (eds) (1996). Fire and Mud: Eruptions and Lahars of Mount Pinatubo, Philippines. Seattle: University of Washington Press, 1126 p.

Pallister, J. S., Hoblitt, R. P., Meeker, G. P., Knight, R. J. & Siems, D. F. (1996). Magma mixing at Mount Pinatubo: Petrographic and chemical evidence from the 1991 deposits. In: Newhall, C. G. & Punongbayan, R. S. (eds) *Fire and Mud: Eruptions and Lahars of Mount Pinatubo, Philippines*. Seattle: University of Washington Press, 751–766.

Pichavant, M., Costa, F., Burgisser, A., Scaillet, B., Martel, C. & Poussineau, S. (2007). Equilibration Scales in Silicic to Intermediate Magmas Implications for Experimental Studies. *Journal of Petrology* **48**, 1955–1972.

Pouchou, J.-L. & Pichoir, F. (1991). Quantitative Analysis of Homogeneous or Stratified Microvolumes Applying the Model "PAP." In: Heinrich, K. F. J. & Newbury, D. E. (eds) *Electron Probe Quantitation*. Boston, MA: Springer US, 31–75.

Downloaded from https://academic.oup.com/petrology/advance-article/doi/10.1093/petrology/egab027/6188641 by University of Nevada at Reno user on 31 March 2021

Putirka, K. D. (2008). Thermometers and Barometers for Volcanic Systems. *Reviews in Mineralogy and Geochemistry* **69**, 61–120.

Ridolfi, F. & Renzulli, A. (2012). Calcic amphiboles in calc-alkaline and alkaline magmas: thermobarometric and chemometric empirical equations valid up to 1,130°C and 2.2 GPa. *Contributions to Mineralogy and Petrology* **163**, 877–895.

Riker, J. M., Blundy, J. D., Rust, A. C., Botcharnikov, R. E. & Humphreys, M. C. S. (2015). Experimental phase equilibria of a Mount St. Helens rhyodacite: a framework for interpreting crystallization paths in degassing silicic magmas. *Contributions to Mineralogy and Petrology* **170**:6.

Robinson, P., Spear, F. S., Schumacher, J. C., Laird, J., Klein, C., Evans, B. W. & Doolan, B. L. (1982). Phase relations of metamorphic amphiboles: Natural occurrence and theory. *Reviews in Mineralogy* **9B**, 1-228.

Ruprecht, P. & Bachmann, O. (2010). Pre-eruptive reheating during magma mixing at Quizapu volcano and the implications for the explosiveness of silicic arc volcanoes. *Geology* **38**, 919–922.

Ruprecht, P., Bergantz, G. W., Cooper, K. M. & Hildreth, W. (2012). The Crustal Magma Storage System of Volcan Quizapu, Chile, and the Effects of Magma Mixing on Magma Diversity. *Journal of Petrology* **53**, 801–840.

Ruprecht, P. & Cooper, K. M. (2012). Integrating the Uranium-Series and Elemental Diffusion Geochronometers in Mixed Magmas from Volcan Quizapu, Central Chile. *Journal of Petrology* **53**, 841–871.

Ruprecht, P., Simon, A. C. & Fiege, A. (2020). The Survival of Mafic Magmatic Enclaves and the Timing of Magma Recharge. *Geophysical Research Letters* **47**, e2020GL087186.

Rutherford, M. J. (2008). Magma Ascent Rates. *Reviews in Mineralogy and Geochemistry* **69**, 241–271.

Rutherford, M. & Devine, J. (1988). The May 18, 1980, Eruption of Mount St. Helens 3. Stability and Chemistry of Amphibole in the Magma Chamber. *Journal of Geophysical Research-Solid Earth and Planets* **93**, 11949–11959.

Rutherford, M. J. & Devine, J. D. (1996). Pre-eruption pressure-temperature conditions and volatiles in the 1991 dacitic magma of Mount Pinatubo. In: Newhall, C. G. & Punongbayan, R. S. (eds) *Fire and Mud: Eruptions and Lahars of Mount Pinatubo, Philippines*. Seattle: University of Washington Press, 751–766.

Rutherford, M. J. & Devine, J. D. (2003). Magmatic conditions and magma ascent as indicated by hornblende phase equilibria and reactions in the 1995-2002 Soufrière Hills magma. *Journal of Petrology* **44**, 1433–1454.

Rutherford, M. J. & Devine, J. D. (2008). Magmatic conditions and processes in the storage zone of the 2004–2006 Mount St. Helens dacite. In: Sherrod, D. R., Scott, W. E., & Stauffer, P. H. (eds*)* A Volcano Rekindled: The Renewed Eruption of Mount St. Helens, *U.S. Geological Survey Professional Paper* **1750**, 703–725.

Rutherford, M. & Hill, P. (1993). Magma Ascent Rates from Amphibole Breakdown: an Experimental Study Applied to the 1980-1986 Mount St. Helens Eruptions. *Journal of Geophysical Research-Solid Earth* **98**, 19667–19685.

Rutherford, M. J., Sigurdsson, H., Carey, S. & Davis, A. (1985). The May 18, 1980, Eruption of Mount St. Helens 1. Melt Composition and Experimental Phase Equilibria. *Journal of Geophysical Research* **90**, 2929–2947.

Downloaded from https://academic.oup.com/petrology/advance-article/doi/10.1093/petrology/egab027/6188641 by University of Nevada at Reno user on 31 March 2021

Salas, P. A., Rabbia, O. M., Hernández, L. B. & Ruprecht, P. (2017). Mafic monogenetic vents at the Descabezado Grande volcanic field (35.5°S–70.8°W): the northernmost evidence of regional primitive volcanism in the Southern Volcanic Zone of Chile. *International Journal of Earth Sciences* **106**, 1107–1121.

Scaillet, B. & Evans, B. W. (1999). The 15 June 1991 eruption of Mount Pinatubo. I. Phase equilibria and pre-eruption P–T–fO_2–fH_2O conditions of the dacite magma. *Journal of Petrology* **40**, 381–411.

Shea, T. & Hammer, J. E. (2013a). Oxidation in CSPV experiments involving H2O-bearing mafic magmas: Quantification and mitigation. *American Mineralogist* **98**, 1285–1296.

Shea, T. & Hammer, J. E. (2013b). Kinetics of cooling- and decompression-induced crystallization in hydrous mafic-intermediate magmas. *Journal of Volcanology and Geothermal Research* **260**, 127–145.

Spear, F. S. (1981). An experimental study of hornblende stability and compositional variability in amphibole. *American Journal of Science* **281**, 697–734.

Taylor, J. R., Wall, V. J. & Pownceby, M. I. (1992). The calibration and application of accurate redox sensors. *American Mineralogist* **77**, 284–295.

Thomas, M. E. & Neuberg, J. W. (2014). Understanding which parameters control shallow ascent of silicic effusive magma. *Geochemistry, Geophysics, Geosystems* **15**, 4481–4506.

Tomiya, A., Takahashi, E., Furukawa, N. & Suzuki, T. (2010). Depth and Evolution of a Silicic Magma Chamber: Melting Experiments on a Low-K Rhyolite from Usu Volcano, Japan. *Journal of Petrology* **51**, 1333–1354.

Tomkins, A. G., Rebryna, K. C., Weinberg, R. F. & Schaefer, B. F. (2012). Magmatic Sulfide Formation by Reduction of Oxidized Arc Basalt. *Journal of Petrology* **53**, 1537–1567.

Tsuchiyama, A. (1985). Dissolution kinetics of plagioclase in the melt of the system diopside-albite-anorthite, and origin of dusty plagioclase in andesites. *Contributions to Mineralogy and Petrology* **89**, 1–16.

Venezky, D. Y. & Rutherford, M. J. (1999). Petrology and Fe Ti oxide reequilibration of the 1991 Mount Unzen mixed magma. *Journal of Volcanology and Geothermal Research* **89**, 213–230.

Waters, L. E. & Andrews, B. J. (2016). The role of superheating in the formation of Glass Mountain obsidians (Long Valley, CA) inferred through crystallization of sanidine. *Contributions to Mineralogy and Petrology* **171**:79.

Waters, L. E. & Lange, R. A. (2016). No effect of H_2O degassing on the oxidation state of magmatic liquids. *Earth and Planetary Science Letters* **447**, 48–59.

Waters, L. E. & Lange, R. A. (2017). An experimental study of $^{Fe2+-Mg}K_D$ between orthopyroxene and rhyolite: a strong dependence on H_2O in the melt. *Contributions to Mineralogy and Petrology* **172**:42.

Waters, L. E. & Lange, R. A. (2015). An updated calibration of the plagioclase-liquid hygrometer-thermometer applicable to basalts through rhyolites. *American Mineralogist* **100**, 2172–2184.

Welsch, B., Hammer, J., Baronnet, A., Jacob, S., Hellebrand, E. & Sinton, J. (2016). Clinopyroxene in postshield Haleakala ankaramite: 2. Texture, compositional zoning and supersaturation in the magma. *Contributions to Mineralogy and Petrology* **171**:6.

Winslow, H., Ruprecht, P., Stelten, M., Amigo, A. (2020) Evidence for primitive magma storage and eruption following prolonged equilibration in thickened crust. *Bulletin of Volcanology* **82**:69.

http://www.petrology.oupjournals.org/

Downloaded from https://academic.oup.com/petrology/advance-article/doi/10.1093/petrology/egab027/6188641 by University of Nevada at Reno user on 31 March 2021

Wones, D. R. & Eugster, H. P. (1965). Stability of biotite: Experiment, theory, and application. *American Mineralogist* **50**, 1228-1272.

Wyllie, P. J., Donaldson, C. H., Irving, A. J., Kesson, S. E., Merrill, R. B., Presnall, D. C., Stolper, E. M., Usselman, T. M. & Walker, D. (1981). Experimental petrology of basalts and their source rocks. In: Kaula, W. M. (ed) *Basaltic Volcanism on the Terrestrial Planets*. New York: Pergamon Press, 493–630.

Zhang, Y., Xu, Z., Zhu, M. & Wang, H. (2007). Silicate melt properties and volcanic eruptions. *Reviews of Geophysics* **45**, 2006RG000216.

Zhang, Y. (2010). Diffusion in Minerals and Melts: Theoretical Background. *Reviews in Mineralogy and Geochemistry* **72**, 5–59.

Zolotov, M. Yu. & Fegley, B. (1999). Oxidation State of Volcanic Gases and the Interior of Io. *Icarus* **141**, 40–52.

Downloaded from https://academic.oup.com/petrology/advance-article/doi/10.1093/petrology/egab027/6188641 by University of Nevada at Reno user on 31 March 2021

FIGURE CAPTIONS

Figure 1. Location of Volcán Quizapu. Cross-section line for Figure 15 shown in green. Also shown are collection locations of VQ-07-37D pumice (blue dot, IGSN: PPRAI101I) and VQ-06-06 lava (yellow square, IGSN: PPRAI100B). Quizapu crater is to the left of QZ label. Note the similar crater on the north flank of Descabezado Grande. Multiple flows of the 1846-1847 lava are visible, mainly extending to the northwest, with one large flow filling the valley to the southeast. Bright white is snow, and light tan is the 1932 pumice blanket. QZ = Quizapu, CA = Cerro Azul, DG = Descabezado Grande, LH = Los Hornitos (< 2 km directly south of arrow) LS = Loma Seca tuff, RC = Resolana Craters. Labels are immediately right of the feature they describe (LS is directly atop). Overview image at left modified from GeoMapApp; image at right modified from GoogleEarth.

Figure 2. Transmitted light image of Quizapu lava VQ-06-06. The groundmass contains microlites and glass. amph = amphibole, ap = apatite, Fe-Ti ox = iron-titanium oxide (magnetite or ilmenite), opx = orthopyroxene, plag = plagioclase. This photomicrograph shows representative occurrences, but not necessarily proportions, of each key phase in the Quizapu dacite. Pumice samples contain the same phases but lack microlites.

Figure 3. Total alkali-silica diagram of Quizapu starting material (pumice VQ-07-37D), and nearly isochemical lava samples (VQ-06-06 and VQ-06-11). Bulk analyses and VQ-06-11 glass from Ruprecht *et al.*, 2012; VQ-06-06 and VQ-07-37D glass analyses are from this study, via EPMA (Table 3, Table S2). The pumice glass analysis is the first glass geochemistry reported for a 1932 pumice.

Figure 4. BSE images of orthopyroxene in starting materials. (a) Subhedral, unzoned orthopyroxene in pumice VQ-07-37D. (b-d) Reversely zoned orthopyroxene in the lava, with pink arrows indicating subtle growth textures. ap = apatite, gl = glass, mt = magnetite, opx = orthopyroxene.

Downloaded from https://academic.oup.com/petrology/advance-article/doi/10.1093/petrology/egab027/6188641 by University of Nevada at Reno user on 31 March 2021

Figure 5. Orthopyroxene end-member compositions, divided into three smaller plots for clarity. Crystals in the pumice have no core-rim chemical distinction; all analyses are represented as black circles. Two analyses of glomerocrystic orthopyroxene crystals are shown as hexagons. Crystals in the lava have distinct cores (filled grey symbols) and rims (open grey circles). Experimental analyses are of rims or microlites only, from experiments that fall below the biotite-in curve and within the glass-match region shaded in Figures 12 and 13. Color indicates temperature, with deep red for 900 °C, red for 875 °C, and yellow for 860 °C.

Figure 6. (a-d) BSE images of plagioclase microlites and rims in experimental samples, showing the range of sizes and textures (e) Plagioclase microlites (~An_{20}) in lava VQ-06-06 (f) Diagram showing experiments whose direct starting material was pumice VQ-07-37D. Filled circles are samples containing abundant plagioclase microlites and rims; open circles are samples with rare to no microlites or BSE-evident growth rims. The band dividing these two regions delineates the zone of equilibrium plagioclase composition for the Quizapu magma.

Figure 7. Temperature and fO_2 of Quizapu samples calculated from Fe-Ti oxide compositional pairs in Mg/Mn equilibrium (Bacon & Hirschmann, 1988), using the formulation of Ghiorso & Evans (2008). "Lava" refers to VQ-06-06, "pumice" to VQ-07-37D, and "pumice*" to VQ-06-17, a 1932 eruption sample of nearly identical bulk composition toVQ-07-37D. For the Ruprecht *et al.* (2012) data (except VQ-06-17), the average V and Mn values from our own analyses were used, to eliminate differences due to EPMA interferences (see text).

Figure 8. Backscatter electron (BSE) images of Fe-Ti oxides in the starting materials (lava a, b, d; pumice c). The zoning in (a) and (b) is visible only at maximum contrast, and EPMA analyses of the different zones do not yield significantly different compositions (see Figure S7). The trellis feature in (c) is interpreted as rapid oxyexsolution during the 1932 eruption. The Fe oxide in (d) is the same grain as the bright phase in (b), interpreted as a former Fe sulfide that lost S on degassing. The darker grey near the top of the grain is an area richer in Ti, and the bright white area in the southwest quadrant is a remnant of the original Fe sulfide phase.

Downloaded from https://academic.oup.com/petrology/advance-article/doi/10.1093/petrology/egab027/6188641 by University of Nevada at Reno user on 31 March 2021

Figure 9. BSE images of amphibole crystals in natural samples (a-b) and experiments (c-f). Growth rims are evident in the crystals in (c-d), where amphibole is a stable phase. In (d), two distinct generations of amphibole growth are visible, from the multi-step trajectory of the material. In (e-f), amphibole is unstable, as evidenced by its irregular, rounded shapes and association with pyroxene.

Figure 10. BSE images of experimentally-grown biotite, in the groundmass (a) and surrounding destabilized orthopyroxene (b-d).

Figure 11. Trends in residual experimental glass compositions for P_{H2O} = 125 MPa. All experimental analyses used in the regression are plotted. R-squared values refer to the linear least-squares fit to experimental averages, shown as a solid line; dashed lines are linear least-squares fits to ±1σ variance of the data. Horizontal solid lines mark the Quizapu pumice glass composition, with 1σ variance shown by the shaded band. The intersection of natural and experimental trends gives the temperature at which the natural glass composition is best matched at P = 125 MPa, for the given oxide. The plots in this figure are examples of six of the 59 individual regressions with $R^2 \geq 0.75$ used to determine the global glass compositional match in Figure 12 (and shown as open circles in that figure). See methodological details in the Supplementary Methods and additional plots in Figure S13.

Figure 12. Compositional match between experimental residual glass compositions and Quizapu pumice glass composition. Each of the best match P_{H2O}-T points from the 59 individual regressions used (examples shown in Figure 11) are plotted as open circles, with size determined by weight factor assigned to determine average best match for a given P_{H2O} or T. This average best fit at each T or P_{H2O} is shown as a star. Solid line is global best estimate of P_{H2O}-T range for the closest match. Dark dot-dash line is fit to data from pressure regression averages (dark stars), and lighter dashed line is fit to data from temperature regression averages (light stars). See details in the Supplementary Methods.

Figure 13. Phase diagram for Quizapu dacite at H_2O-saturated conditions and an fO_2 of ~NNO+0.2. Symbols indicate the direction of approach to equilibrium, with shaded corners

Downloaded from https://academic.oup.com/petrology/advance-article/doi/10.1093/petrology/egab027/6188641 by University of Nevada at Reno user on 31 March 2021

landing on the actual experimental conditions. Phase labels are written on the mineral-in (stable) side of curves. Minimum plagioclase anorthite (An) content is written above the corresponding experimental symbol. Apatite is stable at all experimental conditions. Orthopyroxene is stable in all experiments outside the biotite field. Light grey dotted lines mark H_2O solubility contours for Quizapu melt (VQ-07-37D glass), calculated using equation 10 of Zhang *et al.*, 2007. Shaded light grey region is where Quizapu pumice glass composition is reproduced in experiments; this is the same region derived in Figure 12 and associated text. Shaded darker grey region is the experimentally determined estimate of long-term storage conditions before both the 1846-1847 and 1932 eruptions. Contrast with Figure 14.

Figure 14. As Figure 13, but for fO_2 = NNO-2. Axes cover the same ranges as previous figure. Note large shift in amphibole and biotite stability curves. Plagioclase, apatite, and Fe sulfide are stable across all experimental conditions. Magnetite and ilmenite are either unstable or undergoing extreme chemical diffusion in every run (Figure S16), interpreted as an effect of the large fO_2 difference from the starting materials. For these experiments, the glass match area was calculated only for the region of the phase diagram where amphibole is stable, but it would presumably extend to lower pressures and higher temperatures, as in Figure 13.

Figure 15. True-scale elevation profile and sub-surface schematic of magma chamber depths and relative sizes. For simplicity's sake, underlying mush and other features are not included. Labels "A" and "B" correspond to the marked transect in Figure 1. Data for elevation profile from Google Terrain. If we assume a spherical chamber centered at 4 km depth, directly below Quizapu crater, this figure illustrates how different volumes of magma would be situated with respect to Quizapu and its surroundings. See text for discussion.

Figure 16. BSE images of an amphibole crystal in lava VQ-06-06 that shows incipient destabilization, including rounding (a), and edge roughness in contact with anhydrous phases (b). Panel (b) is a close-up of the area outlined in a white box in (a).

Downloaded from https://academic.oup.com/petrology/advance-article/doi/10.1093/petrology/egab027/6188641 by University of Nevada at Reno user on 31 March 2021

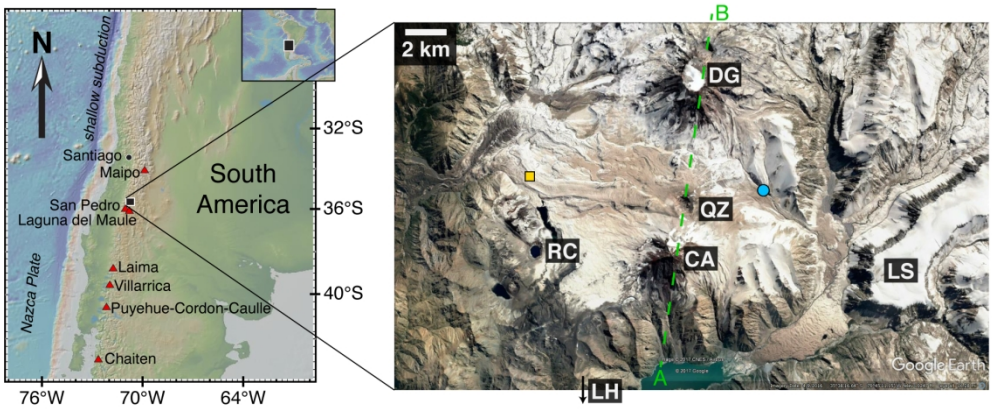

Figure 1. Location of Volcán Quizapu. Cross-section line for Figure 15 shown in green. Also shown are collection locations of VQ-07-37D pumice (blue dot, IGSN: PPRAI101I) and VQ-06-06 lava (yellow square, IGSN: PPRAI100B). Quizapu crater is to the left of QZ label. Note the similar crater on the north flank of Descabezado Grande. Multiple flows of the 1846-1847 lava are visible, mainly extending to the northwest, with one large flow filling the valley to the southeast. Bright white is snow, and light tan is the 1932 pumice blanket. QZ = Quizapu, CA = Cerro Azul, DG = Descabezado Grande, LH = Los Hornitos (< 2 km directly south of arrow) LS = Loma Seca tuff, RC = Resolana Craters. Labels are immediately right of the feature they describe (LS is directly atop). Overview image at left modified from GeoMapApp; image at right modified from GoogleEarth.

Downloaded from https://academic.oup.com/petrology/advance-article/doi/10.1093/petrology/egab027/6188641 by University of Nevada at Reno user on 31 March 2021

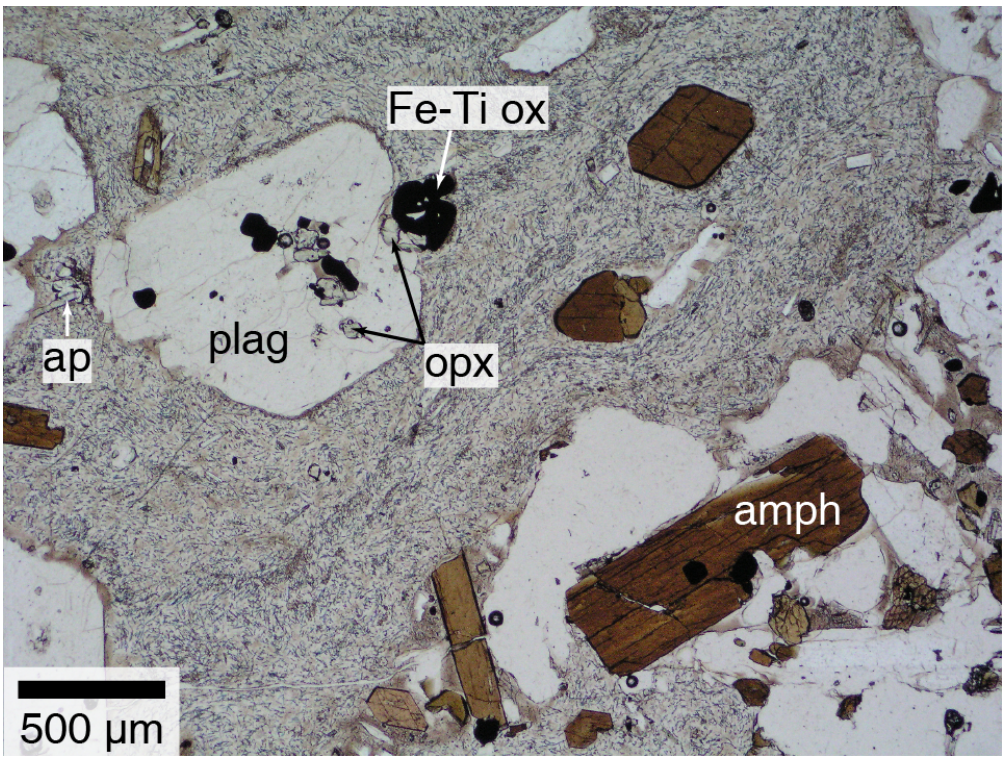

Figure 2. Transmitted light image of Quizapu lava VQ-06-06. The groundmass contains microlites and glass. amph = amphibole, ap = apatite, Fe-Ti ox = iron-titanium oxide (magnetite or ilmenite), opx = orthopyroxene, plag = plagioclase. This photomicrograph shows representative occurrences, but not necessarily proportions, of each key phase in the Quizapu dacite. Pumice samples contain the same phases but lack microlites.

Downloaded from https://academic.oup.com/petrology/advance-article/doi/10.1093/petrology/egab027/6188641 by University of Nevada at Reno user on 31 March 2021

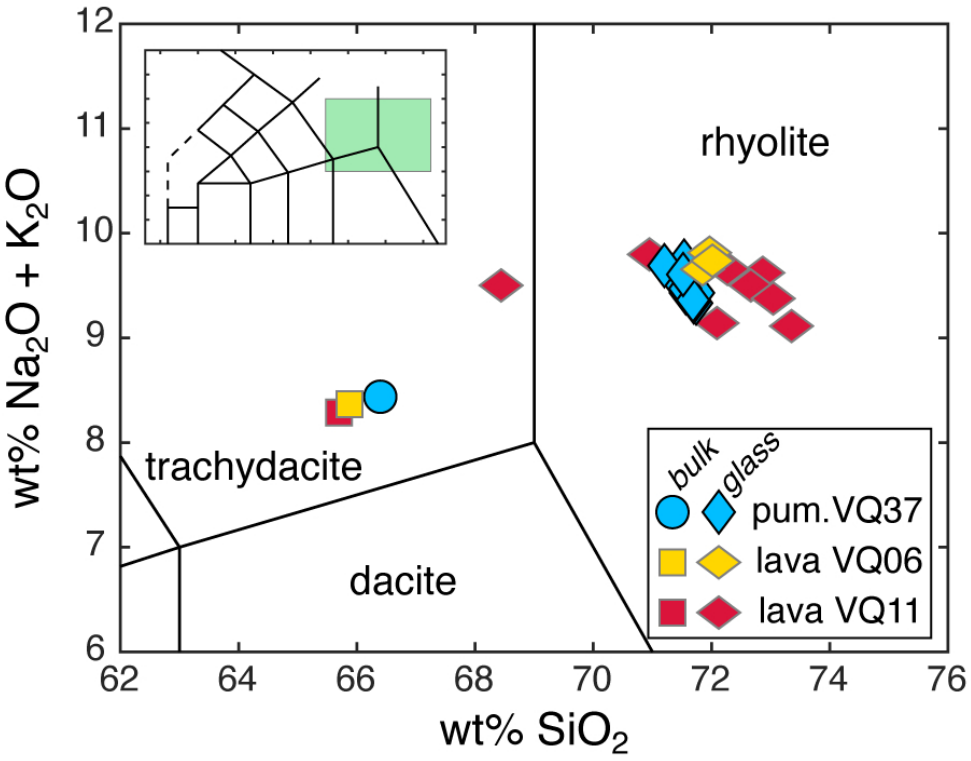

Figure 3. Total alkali-silica diagram of Quizapu starting material (pumice VQ-07-37D), and nearly isochemical lava samples (VQ-06-06 and VQ-06-11). Bulk analyses and VQ-06-11 glass from Ruprecht et al., 2012; VQ-06-06 and VQ-07-37D glass analyses are from this study, via EPMA (Table 3, Table S2). The pumice glass analysis is the first glass geochemistry reported for a 1932 pumice.

Downloaded from https://academic.oup.com/petrology/advance-article/doi/10.1093/petrology/egab027/6188641 by University of Nevada at Reno user on 31 March 2021

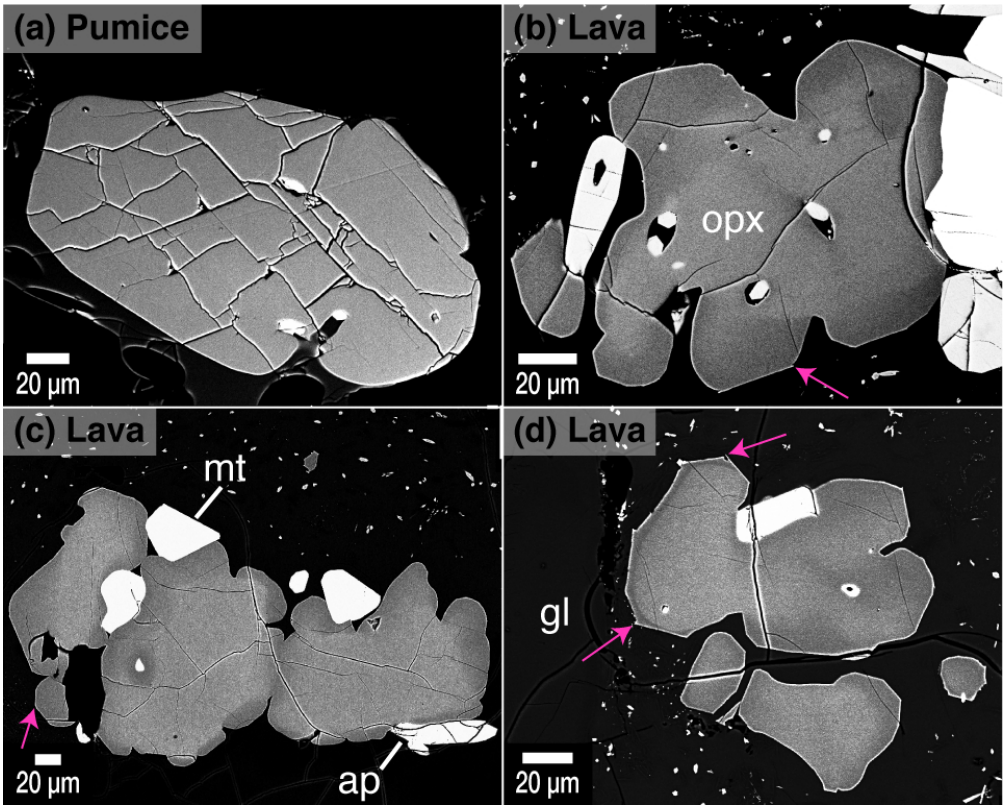

Figure 4. BSE images of orthopyroxene in starting materials. (a) Subhedral, unzoned orthopyroxene in pumice VQ-07-37D. (b-d) Reversely zoned orthopyroxene in the lava, with pink arrows indicating subtle growth textures. ap = apatite, gl = glass, mt = magnetite, opx = orthopyroxene.

Downloaded from https://academic.oup.com/petrology/advance-article/doi/10.1093/petrology/egab027/6188641 by University of Nevada at Reno user on 31 March 2021

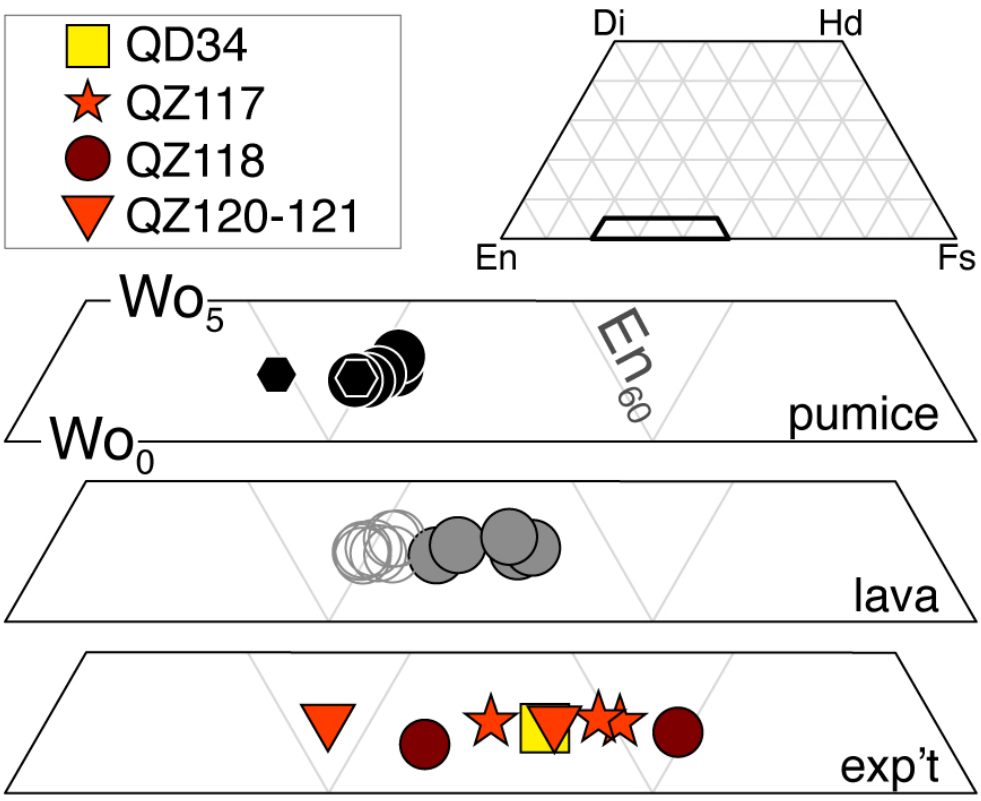

Figure 5. Orthopyroxene end-member compositions, divided into three smaller plots for clarity. Crystals in the pumice have no core-rim chemical distinction; all analyses are represented as black circles. Two analyses of glomerocrystic orthopyroxene crystals are shown as hexagons. Crystals in the lava have distinct cores (filled grey symbols) and rims (open grey circles). Experimental analyses are of rims or microlites only, from experiments that fall below the biotite-in curve and within the glass-match region shaded in Figures 12 and 13. Color indicates temperature, with deep red for 900 °C, red for 875 °C, and yellow for 860 °C.

Downloaded from https://academic.oup.com/petrology/advance-article/doi/10.1093/petrology/egab027/6188641 by University of Nevada at Reno user on 31 March 2021

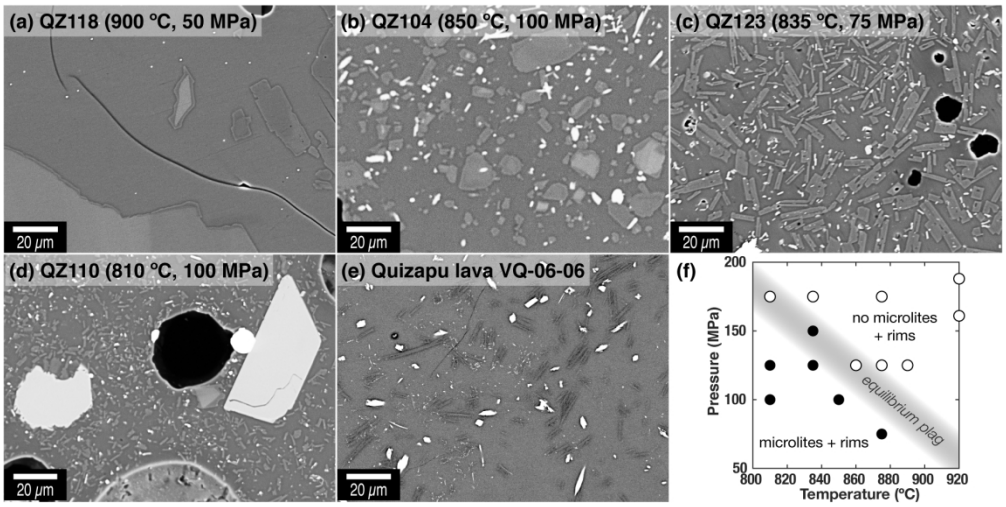

Figure 6. (a-d) BSE images of plagioclase microlites and rims in experimental samples, showing the range of sizes and textures (e) Plagioclase microlites (~An_{20}) in lava VQ-06-06 (f) Diagram showing experiments whose direct starting material was pumice VQ-07-37D. Filled circles are samples containing abundant plagioclase microlites and rims; open circles are samples with rare to no microlites or BSE-evident growth rims. The band dividing these two regions delineates the zone of equilibrium plagioclase composition for the Quizapu magma.

Downloaded from https://academic.oup.com/petrology/advance-article/doi/10.1093/petrology/egab027/6188641 by University of Nevada at Reno user on 31 March 2021

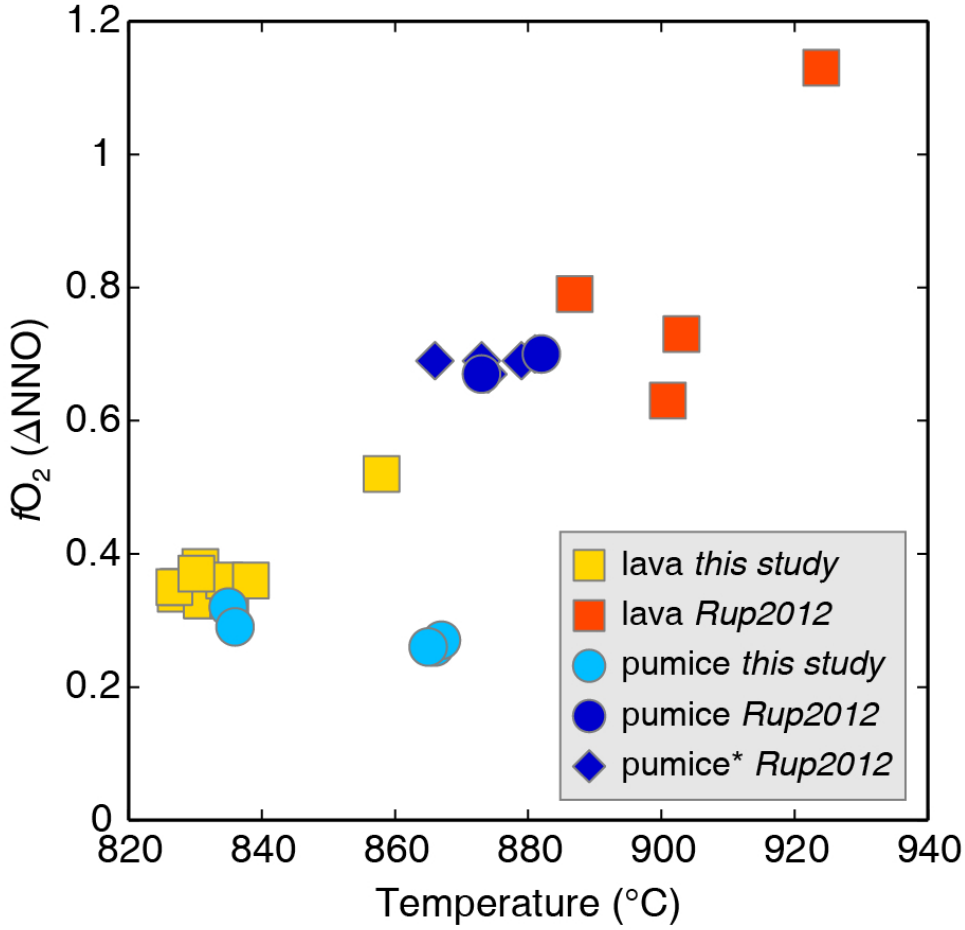

Figure 7. Temperature and fO_2 of Quizapu samples calculated from Fe-Ti oxide compositional pairs in Mg/Mn equilibrium (Bacon & Hirschmann, 1988), using the formulation of Ghiorso & Evans (2008). "Lava" refers to VQ-06-06, "pumice" to VQ-07-37D, and "pumice*" to VQ-06-17, a 1932 eruption sample of nearly identical bulk composition toVQ-07-37D. For the Ruprecht *et al*. (2012) data (except VQ-06-17), the average V and Mn values from our own analyses were used, to eliminate differences due to EPMA interferences (see text).

Downloaded from https://academic.oup.com/petrology/advance-article/doi/10.1093/petrology/egab027/6188641 by University of Nevada at Reno user on 31 March 2021

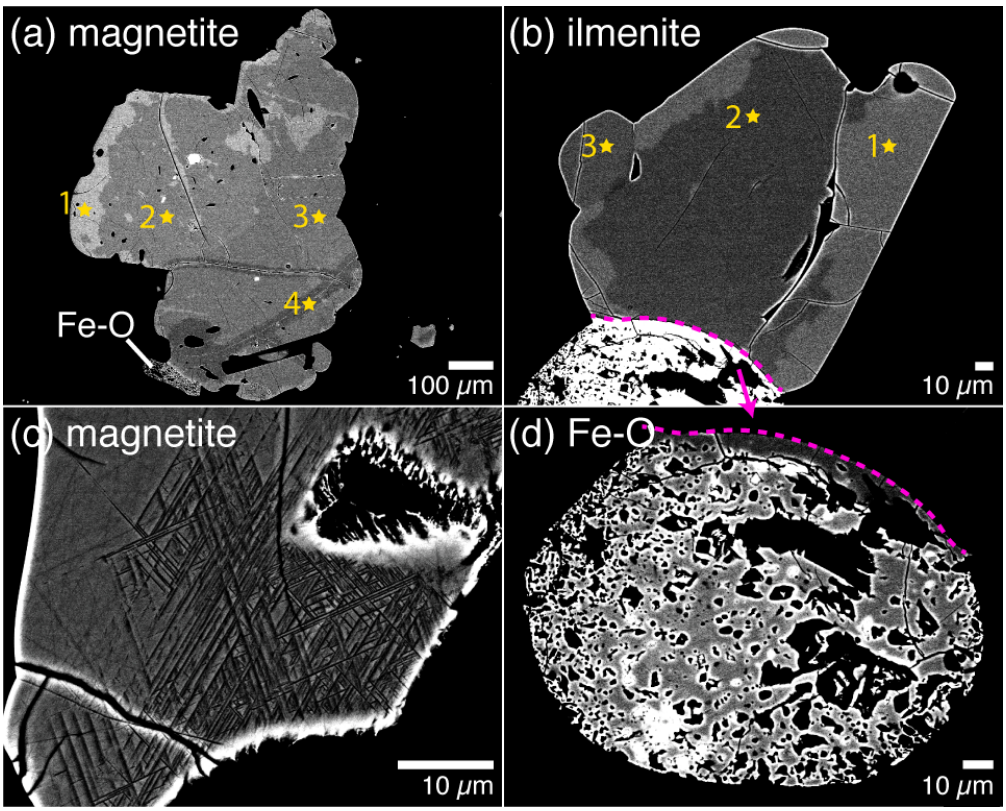

Figure 8. Backscatter electron (BSE) images of Fe-Ti oxides in the starting materials (lava a, b, d; pumice c). The zoning in (a) and (b) is visible only at maximum contrast, and EPMA analyses of the different zones do not yield significantly different compositions (see Figure S7). The trellis feature in (c) is interpreted as rapid oxyexsolution during the 1932 eruption. The Fe-oxide in (d) is the same grain as the bright phase in (b), interpreted as a former Fe sulfide that lost S on degassing. The darker grey near the top of the grain is an area richer in Ti, and the bright white area in the southwest quadrant is a remnant Fe-S phase.

81x65mm (300 x 300 DPI)

Downloaded from https://academic.oup.com/petrology/advance-article/doi/10.1093/petrology/egab027/6188641 by University of Nevada at Reno user on 31 March 2021

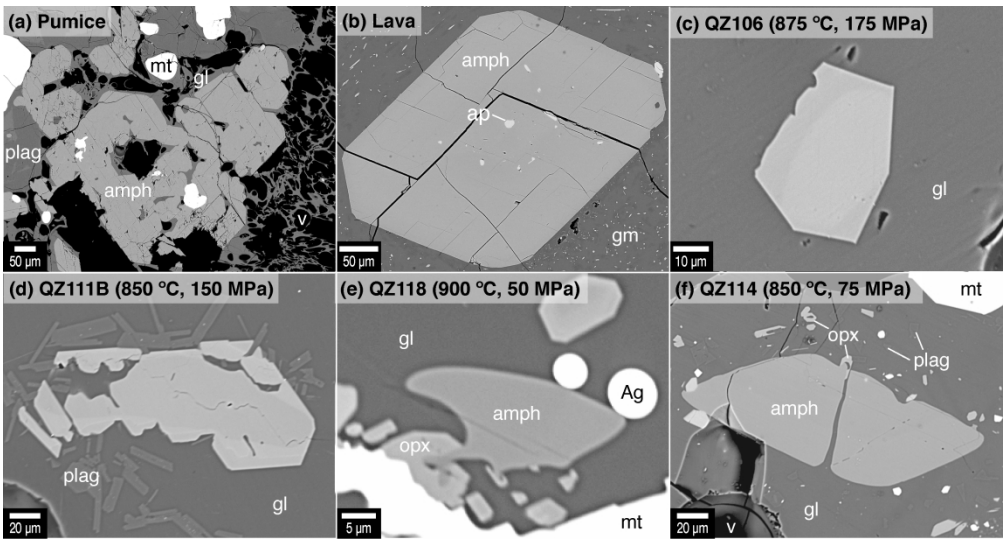

Figure 9. BSE images of amphibole crystals in natural samples (a-b) and experiments (c-f). Growth rims are evident in the crystals in (c-d), where amphibole is a stable phase. In (d), two distinct generations of amphibole growth are visible, from the multi-step trajectory of the material. In (e-f), amphibole is unstable, as evidenced by its irregular, rounded shapes and association with pyroxene.

165x88mm (535 x 535 DPI)

Downloaded from https://academic.oup.com/petrology/advance-article/doi/10.1093/petrology/egab027/6188641 by University of Nevada at Reno user on 31 March 2021

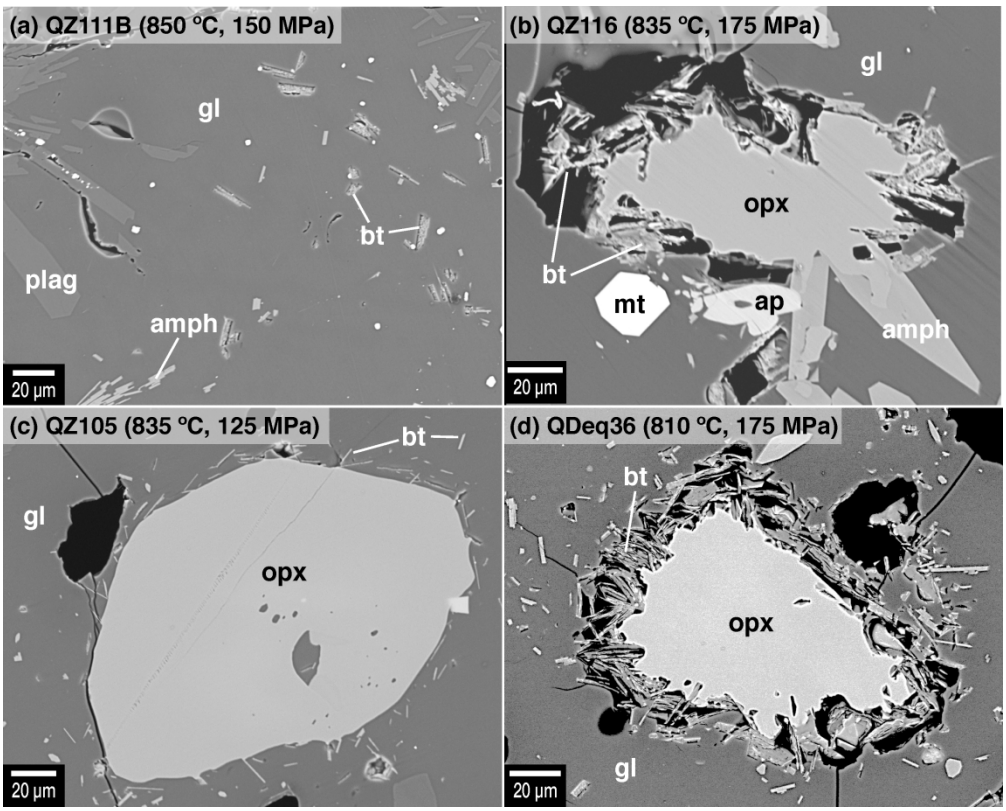

Figure 10. BSE images of experimentally-grown biotite, in the groundmass (a) and surrounding destabilized orthopyroxene (b-d).

165x132mm (471 x 471 DPI)

Downloaded from https://academic.oup.com/petrology/advance-article/doi/10.1093/petrology/egab027/6188641 by University of Nevada at Reno user on 31 March 2021

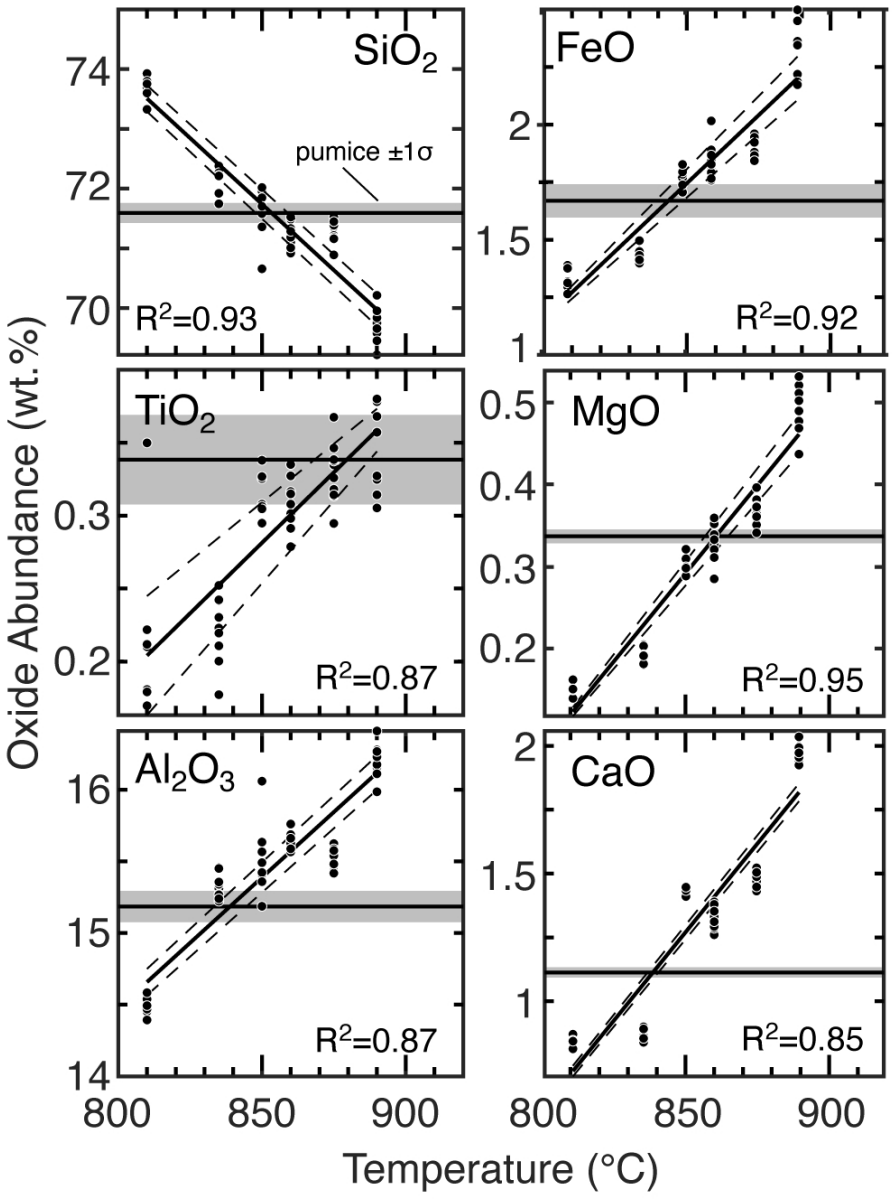

Figure 11. Trends in residual experimental glass compositions for PH_2O = 125 MPa. All experimental analyses used in the regression are plotted. R-squared values refer to the linear least-squares fit to experimental averages, shown as a solid line; dashed lines are linear least-squares fits to ±1σ variance of the data. Horizontal solid lines mark the Quizapu pumice glass composition, with 1σ variance shown by the shaded band. The intersection of natural and experimental trends gives the temperature at which the natural glass composition is best matched at P = 125 MPa, for the given oxide. The plots in this figure are examples of six of the 59 individual regressions with $R^2 \geq 0.75$ used to determine the global glass compositional match in Figure 12 (and shown as open circles in that figure). See methodological details in the Supplementary Methods and additional plots in Figure S13.

Downloaded from https://academic.oup.com/petrology/advance-article/doi/10.1093/petrology/egab027/6188641 by University of Nevada at Reno user on 31 March 2021

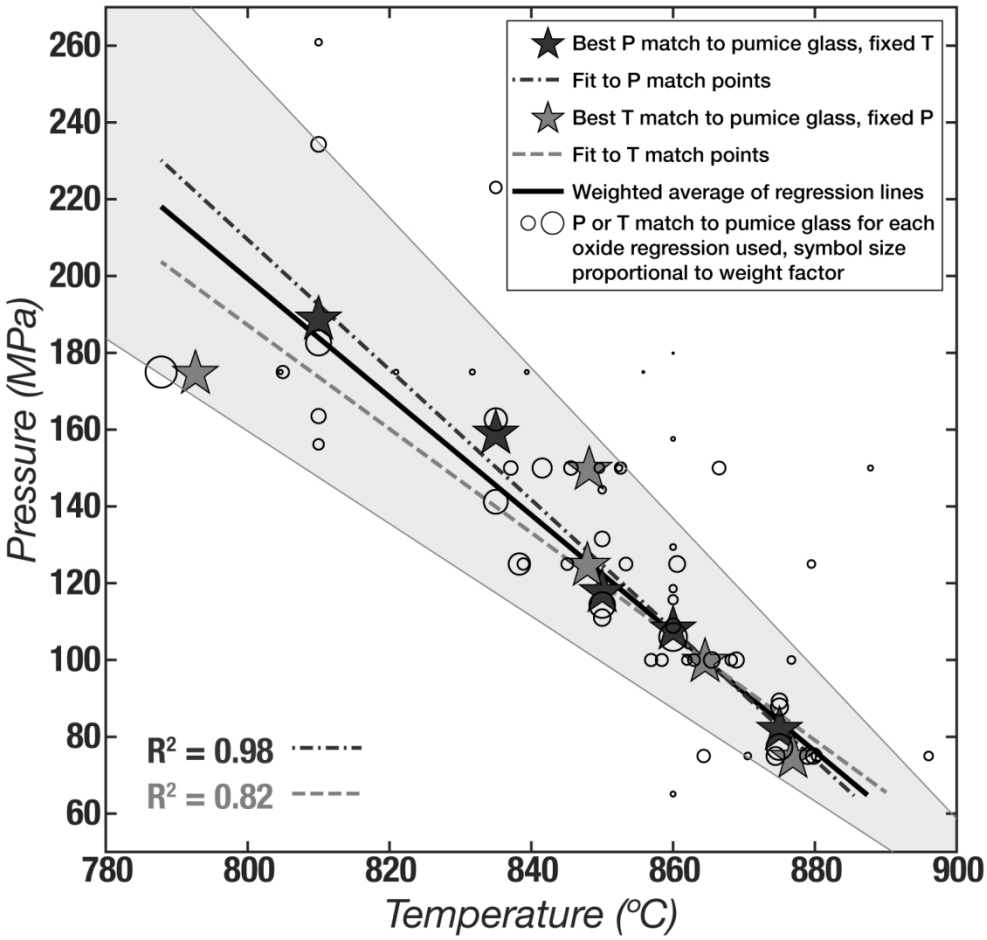

Figure 12. Compositional match between experimental residual glass compositions and Quizapu pumice glass composition. Each of the best match PH_2O-T points from the 59 individual regressions used (examples shown in Figure 11) are plotted as open circles, with size determined by weight factor assigned to determine average best match for a given PH_2O or T. This average best fit at each T or PH_2O is shown as a star. Solid line is global best estimate of PH_2O-T range for the closest match. Dark dot-dash line is fit to data from pressure regression averages (dark stars), and lighter dashed line is fit to data from temperature regression averages (light stars). See details in the Supplementary Methods.

Downloaded from https://academic.oup.com/petrology/advance-article/doi/10.1093/petrology/egab027/6188641 by University of Nevada at Reno user on 31 March 2021

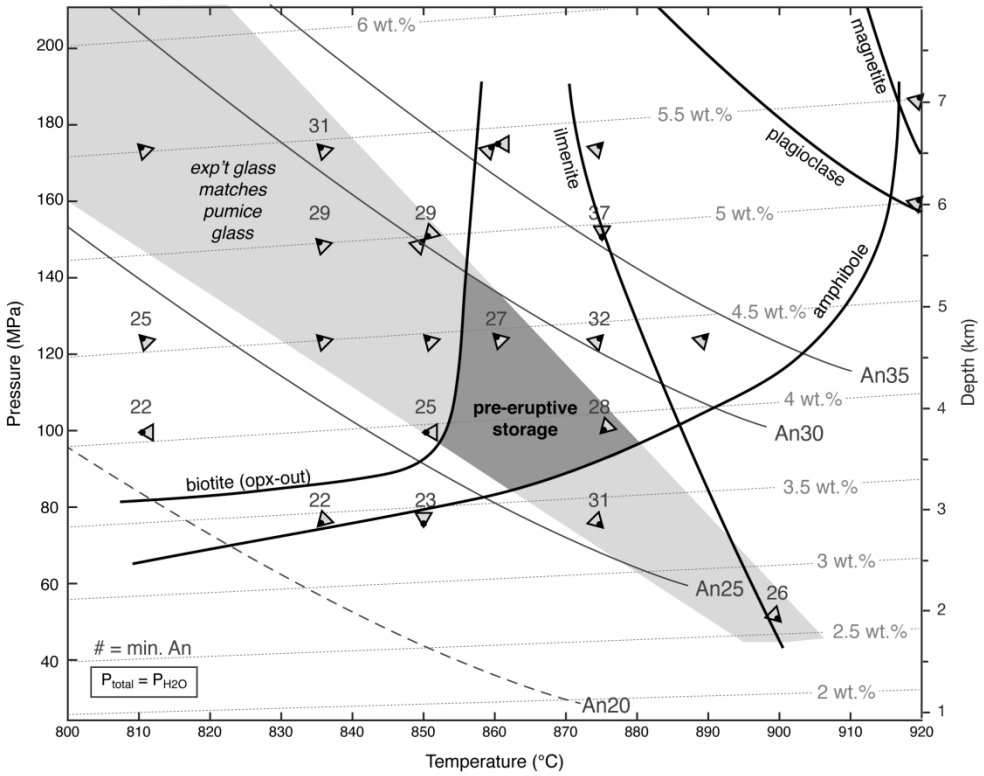

Figure 13. Phase diagram for Quizapu dacite at H_2O-saturated conditions and an fO_2 of ~NNO+0.2. Symbols indicate the direction of approach to equilibrium, with shaded corners landing on the actual experimental conditions. Phase labels are written on the mineral-in (stable) side of curves. Minimum plagioclase anorthite (An) content is written above the corresponding experimental symbol. Apatite is stable at all experimental conditions. Orthopyroxene is stable in all experiments outside the biotite field. Light grey dotted lines mark H_2O solubility contours for Quizapu melt (VQ-07-37D glass), calculated using equation 10 of Zhang *et al.*, 2007. Shaded light grey region is where Quizapu pumice glass composition is reproduced in experiments; this is the same region derived in Figure 12 and associated text. Shaded darker grey region is the experimentally determined estimate of long-term storage conditions before both the 1846-1847 and 1932 eruptions. Contrast with Figure 14.

Downloaded from https://academic.oup.com/petrology/advance-article/doi/10.1093/petrology/egab027/6188641 by University of Nevada at Reno user on 31 March 2021

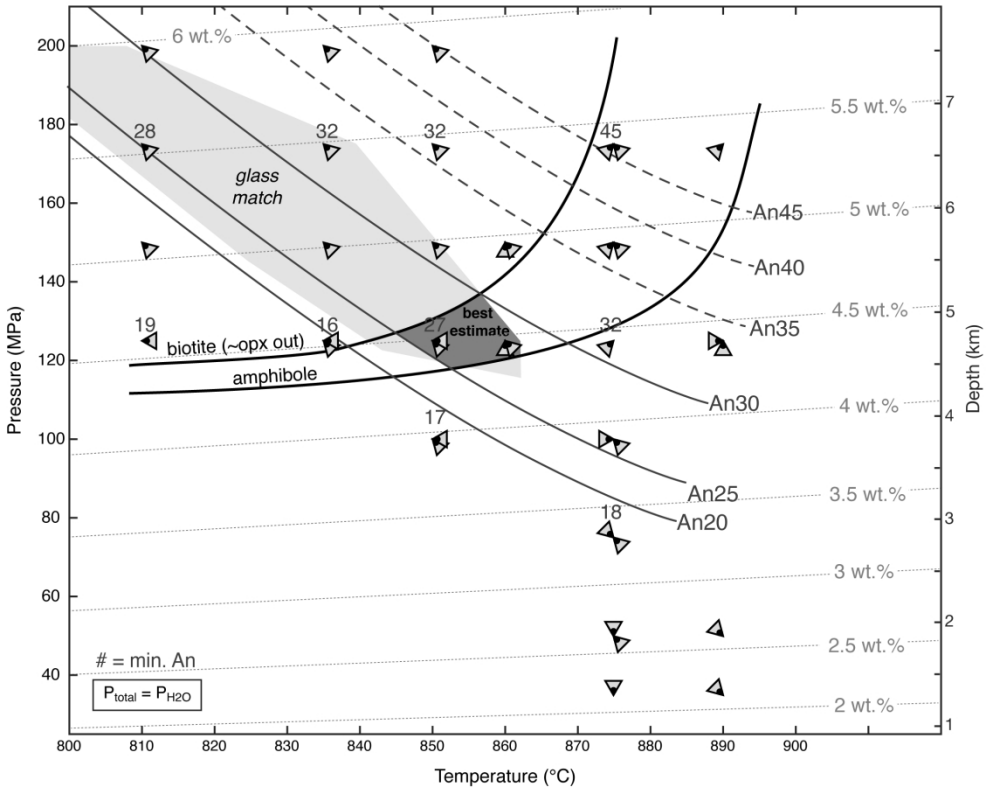

Figure 14. As Figure 13, but for fO_2 = NNO-2. Axes cover the same ranges as previous figure. Note large shift in amphibole and biotite stability curves. Plagioclase, apatite, and Fe-sulfide are stable across all experimental conditions. Magnetite and ilmenite are either unstable or undergoing extreme chemical diffusion in every run, interpreted as an effect of the large fO_2 difference from the starting materials. For these experiments, the glass match area was calculated only for the region of the phase diagram where amphibole is stable, but it would presumably extend to lower pressures and higher temperatures, as in Figure 13.

Downloaded from https://academic.oup.com/petrology/advance-article/doi/10.1093/petrology/egab027/6188641 by University of Nevada at Reno user on 31 March 2021

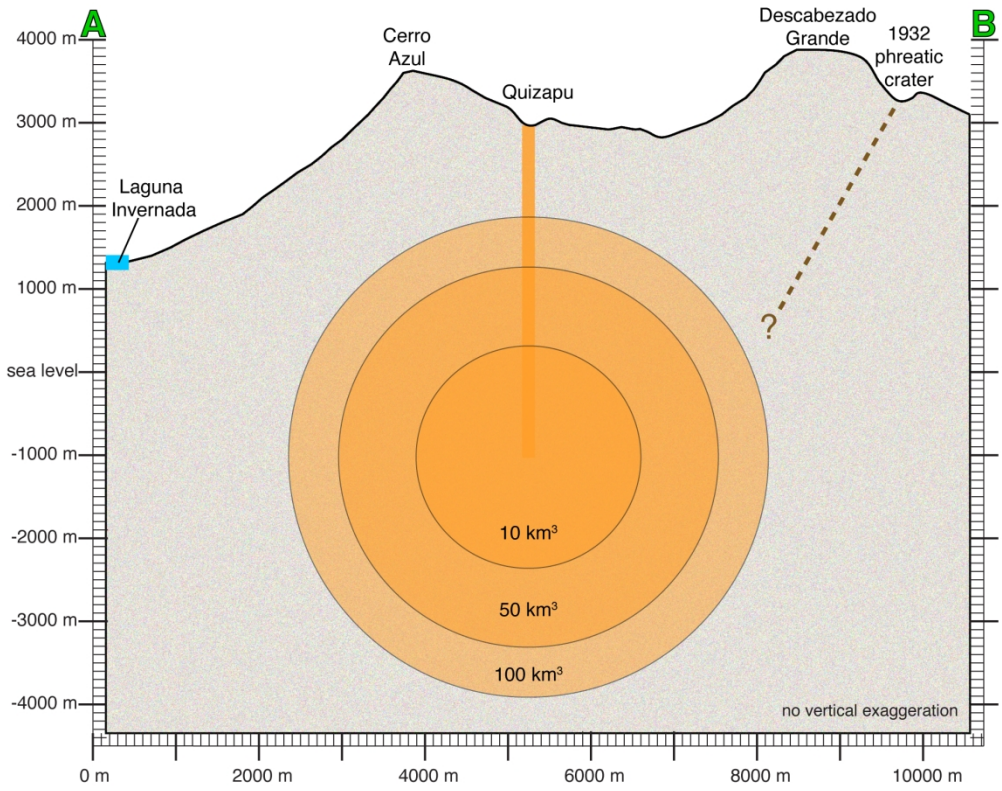

Figure 15. True-scale elevation profile and sub-surface schematic of magma chamber depths and relative sizes. For simplicity's sake, underlying mush and other features are not included. Labels "A" and "B" correspond to the marked transect in Figure 1. Data for elevation profile from Google Terrain. If we assume a spherical chamber centered at 4 km depth, directly below Quizapu crater, this figure illustrates how different volumes of magma would be situated with respect to Quizapu and its surroundings. See text for discussion.

Downloaded from https://academic.oup.com/petrology/advance-article/doi/10.1093/petrology/egab027/6188641 by University of Nevada at Reno user on 31 March 2021

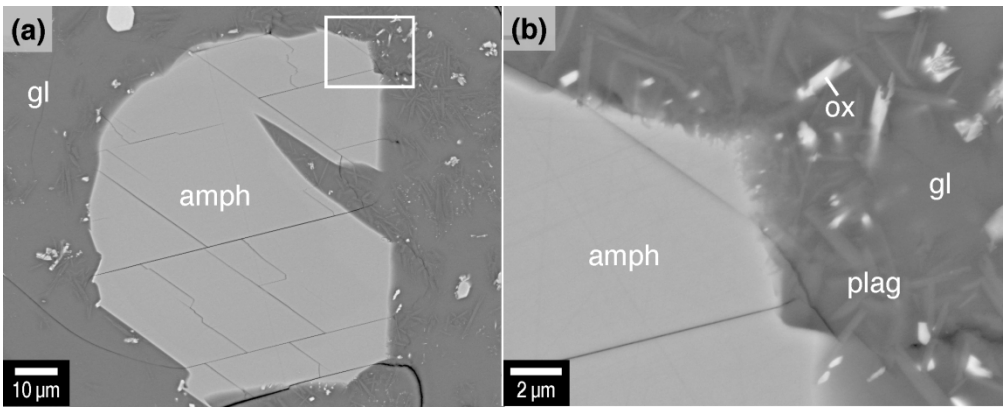

Figure 16. BSE images of an amphibole crystal in lava VQ-06-06 that shows incipient destabilization, including rounding (a), and edge roughness in contact with anhydrous phases (b). Panel (b) is a close-up of the area outlined in a white box in (a).

135x54mm (408 x 408 DPI)

Downloaded from https://academic.oup.com/petrology/advance-article/doi/10.1093/petrology/egab027/6188641 by University of Nevada at Reno user on 31 March 2021

Table 1. Bulk Quizapu materials (wt.%)[a].

	VQ-06-06 lava	VQ-07-37D pumice
IGSN identifier	PPRAI100B	PPRAI101I
Eruption	1846-1847	1932
SiO_2	65.89	66.41
TiO_2	0.56	0.54
Al_2O_3	15.62	15.5
FeO^T	3.09	2.94
MnO	0.09	0.09
MgO	0.95	0.86
CaO	2.48	2.36
Na_2O	5.17	5.15
K_2O	3.19	3.28
P_2O_5	0.15	0.14
Total (dry)	97.2	97.3

a. Data from Table 1 of Ruprecht *et al.*, 2012

Downloaded from https://academic.oup.com/petrology/advance-article/doi/10.1093/petrology/egab027/6188641 by University of Nevada at Reno user on 31 March 2021

Table 2. Experimental run information (fO_2 ~NNO+0.2)

Run ID[a]	Starting Material[b]	T (°C)	P (MPa)	Duration (h)	Stable Crystalline Phases[c, d, e]
QD34[f]	pumice	860	125	338	plag, amph, opx, mt, ilm, ap, cpx
QD35[f]	pumice	835	150	338	plag, amph, bt, mt, ilm, ap, cpx, FeS[e]
QD36[f]	pumice	810	175	337.5	plag, amph, bt, mt, ilm, ap, cpx
QZ-100	pumice	875	125	90	plag, amph, opx, mt, ilm, ap, AgS
QZ-102	QZ-100	850	125	240	plag, amph, mt, ilm, ap, cpx, AgS
QZ-104	pumice	850	100	336	plag, amph, bt, mt, ilm, ap, cpx
QZ-105	pumice	835	125	336	plag, amph, bt, mt, ilm, ap, cpx, AgS
QZ-106	pumice	875	175	168	plag, amph, opx, mt, ap
QZ-107A	QZ-104	860	175	287	plag, amph, opx, mt, ilm, ap, cpx
QZ-107B[g]	QZ106	860	175	287	plag, amph, mt, ap
QZ-108	pumice	810	125	338.5	plag, amph, bt, mt, ilm, ap
QZ-109	pumice	890	125	122	plag, amph, opx, ap
QZ-110	pumice	810	100	269	plag, amph, bt, mt, ap, cpx
QZ-111A	QZ-108	850	150	336	plag, amph, bt, mt, ap, cpx, AgS
QZ-111B	QZ-107A	850	150	336	plag, amph, bt, mt, ilm, ap, cpx
QZ-112	QZ-106	875	150	240.5	plag, amph, opx, mt, ilm, ap, cpx, AgS
QZ-114	QZ-104	850	75	333.5	plag, opx, mt, ilm, ap, cpx, AgS
QZ-115	QZ-105	875	75	288	plag, mt, ilm, ap, cpx
QZ-116	pumice	835	175	337	plag, amph, bt, mt, ilm, ap, AgS
QZ-117	pumice	875	75	332	plag, opx, mt, ilm, ap
QZ-118	QZ-117	900	50	47	plag, opx, mt, ap, AgS
QZ-119	pumice	920	188	24	opx, ap, cpx, AgS
QZ-120	QZ-119	875	100	48.5	plag, amph, opx, mt, ilm, ap, cpx
QZ-121	QZ-120A	875	100	144	plag, amph, opx, mt, ap, cpx
QZ-122[h]	pumice	920	161	24	amph?, opx, mt, ap, sp
QZ-123	QZ122	835	75	193	plag, amph, opx, mt, ilm, ap, cpx

a. Run ID "B" indicates secondary capsule within primary "A" capsule.

b. "Pumice" means sample VQ-07-37D, referenced throughout this article as the natural comparison rock.

c. All experiments contain glass and vesicles.

d. plag = plagioclase, amph = amphibole, bt = biotite, opx = orthopyroxene, mt = titanomagnetite, ilm = hemoilmenite, ap = apatite, cpx = clinopyroxne, sp = spinel, FeS = Fe sulfide, AgS = silver sulfide

e. Sulfides were AgS rather than FeS, in all but one experiment. Though manual searches were conducted, it is possible that sulfides were not identified in every experiment in which they occur, due to their small size.

f. These three experiments were run at the University of Hawaii (UH); the rest were run at Brown University.

g. The lack of pyroxene and ilmenite is likely due to the small size of this "B" experiment (sampling issue).

h. The experimental section observed contains a single amphibole crystal, interpreted as a relict phenocryst. Many parts of the crystal are embayed or rounding, but there are subtle edges and corners whose BSE appearance is consistent with growth. Given the low abundance and uncertainty of interpretation, it is clear that these experimental conditions lie close to the amphibole stability curve, whether just above or just below it.

Downloaded from https://academic.oup.com/petrology/advance-article/doi/10.1093/petrology/egab027/6188641 by University of Nevada at Reno user on 31 March 2021

Downloaded from https://academic.oup.com/petrology/advance-article/doi/10.1093/petrology/egab027/6188641 by University of Nevada at Reno user on 31 March 2021

http://www.petrology.oupjournals.org/

Table 3. Average matrix glass compositions (wt.%) of Quizapu rocks and high fO_2 experimental samples, measured by EPMA.[a]

Sample ID	T (°C)	P (MPa)	n	SiO_2	TiO_2	Al_2O_3	FeO	MnO	MgO	CaO	Na_2O	K_2O	P_2O_5	Cl	O=Cl	H_2O Sol.[b]	Total[c]
QZ100	875	125	10	71.25	0.33	15.52	1.90	0.02	0.37	1.47	5.24	3.82	0.00	0.10	0.02	4.50	99.63
				0.18	0.02	0.07	0.05	0.05	0.02	0.03	0.21	0.05	0.00	0.01			
QZ102	850	125	8	71.56	0.31	15.52	1.78	0.00	0.30	1.43	5.22	3.82	0.00	0.07	0.02	4.57	99.42
				0.44	0.01	0.26	0.04	0.00	0.01	0.01	0.26	0.04	0.00	0.01			
QZ104	850	100	10	73.02	0.23	14.77	1.46	0.00	0.19	0.86	5.05	4.40	0.00	0.05	0.01	4.02	99.10
				0.22	0.02	0.13	0.06	0.00	0.01	0.05	0.14	0.04	0.00	0.03			
QZ106	835	125	10	72.14	0.22	15.32	1.44	0.04	0.19	0.87	5.36	4.43	0.00	0.00	0.00	4.61	99.77
				0.20	0.02	0.08	0.03	0.05	0.01	0.02	0.15	0.08	0.00	0.00			
QZ106	875	175	10	68.62	0.39	16.66	2.36	0.04	0.65	2.28	5.45	3.43	0.03	0.13	0.03	5.49	99.95
				0.86	0.05	0.37	0.16	0.05	0.04	0.17	0.24	0.06	0.05	0.01			
QZ107A	860	175	9	68.93	0.31	16.99	1.84	0.00	0.38	1.91	5.82	3.81	0.00	0.00	0.00	5.53	99.25
				0.74	0.05	0.53	0.07	0.00	0.03	0.13	0.18	0.07	0.00	0.01			
QZ107B	860	175	9	69.36	0.37	16.66	2.12	0.03	0.46	2.08	5.40	3.49	0.02	0.00	0.00	5.52	98.91
				0.54	0.03	0.35	0.05	0.05	0.01	0.08	0.14	0.04	0.04	0.00			
QZ108	810	125	9	73.70	0.21	14.49	1.33	0.00	0.15	0.84	5.06	4.13	0.00	0.11	0.03	4.67	99.19
				0.17	0.06	0.05	0.05	0.00	0.01	0.02	0.16	0.04	0.00	0.01			
QZ109	890	125	10	69.70	0.35	16.21	2.32	0.03	0.50	1.97	5.27	3.63	0.00	0.04	0.01	4.47	99.57
				0.27	0.03	0.11	0.13	0.05	0.03	0.03	0.16	0.03	0.00	0.02			
QZ110	810	100	7	75.44	0.19	14.23	0.85	0.00	0.12	0.66	3.89	4.60	0.00	0.02	0.00	4.13	99.30
				1.09	0.03	0.72	0.10	0.00	0.03	0.27	0.45	0.25	0.00	0.03			
QZ111A	850	150	10	71.34	0.31	15.84	1.47	0.02	0.28	1.38	5.39	3.98	0.00	0.00	0.00	5.07	99.78
				0.30	0.03	0.11	0.05	0.04	0.01	0.03	0.19	0.04	0.00	0.00			
QZ111B	850	150	10	70.70	0.27	16.20	1.45	0.00	0.26	1.30	5.69	4.11	0.01	0.00	0.00	5.07	99.91
				0.26	0.03	0.17	0.05	0.00	0.01	0.03	0.24	0.04	0.03	0.00			
QZ112	875	150	10	68.96	0.30	16.87	2.11	0.05	0.37	1.79	5.72	3.83	0.01	0.00	0.00	5.01	99.65
				0.31	0.05	0.29	0.04	0.05	0.01	0.06	0.07	0.06	0.03	0.00			
QZ114	850	75	11	73.21	0.27	14.56	1.46	0.00	0.20	0.75	5.01	4.50	0.00	0.05	0.01	3.42	99.54
				0.21	0.05	0.09	0.06	0.00	0.02	0.03	0.16	0.06	0.00	0.02			
QZ115	875	75	10	68.64	0.35	16.85	1.74	0.00	0.23	0.63	6.59	4.98	0.00	0.00	0.00	3.36	100.11
				0.41	0.04	0.15	0.10	0.00	0.03	0.06	0.27	0.09	0.00	0.00			
QZ116	835	175	10	71.14	0.29	16.04	1.45	0.00	0.34	1.62	5.31	3.73	0.00	0.08	0.02	5.58	99.74
				0.29	0.03	0.12	0.03	0.00	0.02	0.03	0.17	0.03	0.00	0.01			
QZ117	875	75	10	72.14	0.36	14.91	1.84	0.02	0.29	1.16	5.21	3.99	0.00	0.11	0.03	3.36	99.60

Downloaded from https://academic.oup.com/petrology/advance-article/doi/10.1093/petrology/egab027/6188641 by University of Nevada at Reno user on 31 March 2021

				0.24	0.02	0.06	0.07	0.05	0.02	0.02	0.11	0.05	0.00	0.01			
QZ118	900	50	10	72.08	0.33	14.79	1.95	0.05	0.31	1.08	5.23	4.10	0.00	0.08	0.02	2.62	100.22
				0.24	0.03	0.11	0.08	0.05	0.02	0.03	0.15	0.08	0.00	0.02			
QZ119	920	188	2	70.36	0.43	15.49	2.25	0.00	0.50	1.83	5.43	3.57	0.04	0.13	0.03	5.64	101.38
				0.05	0.04	0.18	0.03	0.00	0.02	0.00	0.14	0.02	0.06	0.01			
QZ120	875	100	10	70.42	0.38	15.60	2.22	0.01	0.43	1.47	5.55	3.81	0.02	0.12	0.03	3.96	99.53
				0.23	0.04	0.10	0.04	0.03	0.01	0.04	0.16	0.07	0.04	0.01			
QZ121	875	100	11	70.98	0.34	15.52	1.89	0.02	0.39	1.32	5.55	3.89	0.02	0.12	0.03	3.96	99.57
				0.15	0.04	0.10	0.08	0.04	0.02	0.02	0.11	0.05	0.03	0.01			
QZ122	920	161	4	70.73	0.39	15.71	1.82	0.03	0.75	2.14	4.97	3.37	0.02	0.10	0.02	5.12	98.72
				1.31	0.04	0.84	0.10	0.05	0.09	0.30	0.25	0.04	0.05	0.01			
QZ123	835	75	15	75.40	0.27	13.53	1.15	0.00	0.20	0.76	4.22	4.37	0.02	0.10	0.02	3.46	99.62
				0.28	0.03	0.09	0.03	0.00	0.01	0.05	0.27	0.05	0.05	0.01			
QDeq34	860	125	10	71.21	0.31	15.64	1.84	0.08	0.33	1.33	5.09	4.04	0.05	0.12	0.03	4.63	99.02
				0.21	0.02	0.06	0.07	0.02	0.02	0.05	0.11	0.04	0.01	0.01			
QDeq35	835	150	9	72.67	0.22	14.94	1.48	0.07	0.21	0.95	5.08	4.27	0.02	0.13	0.03	5.23	100.19
				0.19	0.09	0.08	0.05	0.02	0.02	0.02	0.10	0.02	0.03	0.01			
QDeq36	810	175	10	72.05	0.26	15.57	1.26	0.07	0.24	1.19	5.17	4.07	0.02	0.10	0.02	5.77	99.67
				0.14	0.02	0.05	0.05	0.02	0.02	0.03	0.15	0.03	0.02	0.00			
VQ-06-06[d]	800	50	2	71.98	0.34	15.27	1.57	0.03	0.17	0.85	5.19	4.51	0.00	0.12	0.03	0.11	101.22
				0.11	0.07	0.32	0.13	0.04	0.06	0.01	0.15	0.09	0.00	0.01			
VQ-07-37D[e]	800	50	11	71.59	0.34	15.18	1.67	0.07	0.34	1.11	5.43	4.09	0.04	0.17	0.04	0.11	100.94
				0.17	0.03	0.11	0.07	0.02	0.01	0.02	0.18	0.05	0.02	0.02			

a. Numbers in the second row of each entry indicate 1σ variance in absolute wt.%.

b. H_2O solubility in wt.%, calculated using equation 10 of Zhang *et al.*, 2007.

c. Total as measured, plus H_2O at solubility; only analyses with these totals between 98.5 and 101.5 were accepted. As presented here and in figures, the data have all been normalized to 100 wt.% total to facilitate accurate comparison of the dry melt components.

d. Quizapu lava sample discussed in main text; see Table 1 for whole rock composition.

e. Quizapu pumice sample that was the initial starting material for all higher-fO_2 experiments; see Table 1 for whole rock composition.

Downloaded from https://academic.oup.com/petrology/advance-article/doi/10.1093/petrology/egab027/6188641 by University of Nevada at Reno user on 31 March 2021